D5.10 - Interaction of the tsunami with the seabed. Implications for wind farms, aquaculture, coastal ecosystems and marine protected areas.

Fuhrman, David R.; Eltard-Larsen, Bjarke; Sumer, B. Mutlu; Baykal, Cüneyt; Dogulu, Nilay; Duha Metin, Ayse; Can Aydin, Deniz; Yalciner, Ahmet Cevdet; Omira, Rachid ; Lorenço, Nuno

Total number of authors:
11

Publication date:
2015

Document Version
Publisher's PDF, also known as Version of record

ASTARTE

Assessment, STrategy And Risk Reduction for Tsunamis in Europe

Grant Agreement no: 603839
Organisation name of lead contractor: IPMA
Coordinator: Maria Ana Baptista

Deliverable 5.10

Interaction of the tsunami with the seabed. Implications for wind farms, aquaculture, coastal ecosystems and marine protected areas

Due date of deliverable:	M15
Actual submission date to PC:	Mx15
Start date of the project:	01/11/2013
Duration:	36 months

Work Package:	5 "Tsunami-Coastal Impacts"
Lead beneficiary of this deliverable:	DTU (Partner 19)
Author(s):	**DTU**: David R. Fuhrman, Bjarke Eltard-Larsen, B. Mutlu Sumer, Cuneyt Baykal **METU**: Nilay Dogulu, Ayse Duha Metin, Deniz Can Aydin, Ahmet Cevdet Yalciner **IPMA:** Rachid Omira, Nuno Lorenço, Maria Ana Baptista
Version:	V6

Project co-funded by the European Commission within the Seventh Framework Programme (2007-2013)	
Dissemination Level	
PU Public	X
PP Restricted to other programme participants (including the Commission Services)	
RE Restricted to a group specified by the consortium (including the Commission Services)	
CO Confidential, only for members of the consortium (including the Commission Services)	

TABLE OF CONTENTS

Executive summary 3
Document information 4
Lists of figures and tables 5
Abbreviations and Acronyms 7
Definitions 7
1. Chapter 1: Tsunami-induced scour around monopile wind turbine foundations 8
1.1 Introduction 8
1.2 Hydrodynamic and turbulence model description 9
1.3 Sediment transport and morphological model description 13
1.4 Model validation 15
1.5 Similarity of tsunami field and model scales 20
1.6 Simulation of tsunami-induced scour 25
1.7 Practical model for predicting tsunami-induced scour 29
1.8 Conclusions 31
1.9 References 32
2. Chapter 2: Tsunami impacts on aquaculture 34
2.1 Introduction 34
2.2 Aquaculture 34
2.3 Vulnerability of fisheries and aquaculture systems 36
2.4 Tsunami impacts on aquaculture 37
2.5 Engineering design of aquaculture systems and tsunamis 41
2.6 References 45
3. Chapter 3: Tsunami-impact on coastal ecosystems and marine protected areas 48
3.1 Introduction 48
3.2 Estimating the tsunami impact on coastal ecosystems along the coast of Portugal-NE Atlantic region 48
a. Ecosystems along the coast of Portugal 49
b. Tsunami impact on ecosystems along the coast of Portugal 52
3.3 Conclusions 55
3.4 References 55

EXECUTIVE SUMMARY

In Chapter 1, a fully-coupled (hydrodynamic and morphologic) numerical model is presented, and utilized for the simulation of tsunami-induced scour around a monopile structure, representative of those commonly utilized as offshore wind turbine foundations at moderate depths i.e. for depths <O(30 m). The model is based on solutions to Reynolds-averaged Navier-Stokes equations, coupled with two-equation k-ω turbulence closure, with additional bed and suspended load descriptions forming the basis for sea bed morphology. The model is first validated for flow, bed shear stresses, and scour within a steady current, where a generally excellent match with experimentally-based results is found. A methodology for maintaining and assessing hydrodynamic and morphologic similarity between field and (laboratory) model-scale tsunami events is then presented, combining diameter-based Froude number similarity with that based on the dimensionless wave boundary layer thickness-to-monopile diameter ratio. This methodology is utilized directly in the selection of governing tsunami wave parameters (i.e. velocity magnitude and period) used for subsequent simulation within the numerical model. The flow, sediment transport, and scour processes beneath three tsunami waves are simulated in succession. These illustrate a generally accumulative scour process i.e. a relatively rapid scour induced by the leading wave, with an additional buildup of the scour depth during additional trailing waves. The resulting scour seems to approach an equilibrium value after sufficient time duration, which corresponds reasonably to that predicted by existing steady-current scour depth, after invoking a boundary layer thickness based on the unsteady tsunami wave, i.e. it is important to incorporate both current-like, as well as wave-like aspects of the long tsunami event. Based on the simulated results, a simple methodology for predicting the scour depth in engineering practice is finally developed. This methodology is demonstrated to match the predicted maximum scour for all of the simulated flows considered i.e. ranging from the series of transient tsunami waves to the steady-current limit.

In Chapter 2, the aim is to provide an overview on the tsunami impacts on aquaculture rather than presenting a comprehensive review on the status and trends in aquaculture development. [For such a comprehensive review the reader is referred to the FAO (Food and Agriculture organization of the United Nations) report titled “The State of the World Fisheries and Aquaculture” released in May 2014.] For this purpose, we first briefly provide and introductory summary on aquaculture. This is followed by the section “Vulnerability of Fisheries and Aquaculture Systems” where the main focus is the vulnerability to tsunamis. Next, tsunami Impacts on aquaculture are exemplified based on the major tsunami events that occurred since 2000s. Later, specific case studies highlighting different aspects in aquaculture design are illustrated in the section “Engineering Design of Aquaculture Systems”.

In Chapter 3, tsunami impact on coastal ecosystems is investigated. Ecosystems along the coast of Portugal are considered and a detailed numerical modelling of tsunami impact is performed for the Ria Formosa lagoon (an important ecosystem located in the southern coast of Portugal). The tsunami modelling is carried out using a validated non-linear shallow water numerical code. A high resolution digital elevation model (50m-resolution) of the zone of interest is used to properly simulate the tsunami hazard. The active earthquake sources of the southwest Iberia Margin (SWIM) region represent the tsunamigenic scenarios in this study. Tsunami impact at the Ria Formosa lagoon is assessed through deriving near-shore tsunami wave heights, inundations, and flow velocities. Numerical results show that the Ria Formosa lagoon can suffer powerful tsunami impact due to the occurrence of a tsunami event in the SWIM region.

DOCUMENT INFORMATION

Project Number	FP7 - 603839	**Acronym**	ASTARTE
Full Title	Assessment, STrategy And Risk Reduction forTsunamis in Europe		
Project URL	http://www.astarte-project.eu/		
Document URL			
EU Project Officer	Denis Peter		

Deliverable	**Number**	D5.10	**Title**	
Work Package	**Number**	WP5	**Title**	

Date of Delivery	**Contractual**	M15	**Actual**	Mxx
Status	version 6		final □	
Nature	prototype □ report □ dissemination □			
Dissemination level	public □ consortium □			

Authors (Partner)				
Responsible Author	**Name**		**E-mail**	
	Partner		**Phone**	

Abstract (for dissemination)	This deliverable is comprised of the following three chapters: Chapter 1 presents a detailed CFD numerical study on assessing potential tsunami-induced scour around monopile structures, representative of those commonly utilized as offshore wind turbine foundations. Chapter 2 covers potential tsunami impacts on aquaculture. Vulnerabilities are discussed and exemplified based on major recent tsunamis events, with case studies then used to highlight various aspects important in engineering design. Chapter 3 investigates tsunami impact on coastal ecosystems, including detailed numerical modelling of tsunami impact for the Ria Formosa lagoon, an important ecosystem located in the southern coast of Portugal.
Keywords	Tsunami, scour, wind farms, aquaculture, coastal ecosystems, marine protected areas.

Version Log			
Issue Date	**Rev. No.**	**Author**	**Change**
Oct. 23, 2014	1	DTU	Template
Jan. 29, 2015	2	DTU	Chapter 1 completed
Feb. 3, 2015	3	METU	Chapter 2 incorporated
Feb. 10, 2015	4	DTU	Minor revision to Ch. 1
Mar. 2, 2015	5	IPMA	Chapter 3 incorporated
Mar. 3, 2015	6	DTU	Misc. finishing details

LIST OF FIGURES AND/OR LIST OF TABLES

List of figures:	page
Figure 1.1. Map showing the location of several wind farms within Europe.	9
Figure 1.2. Example computational domain and boundaries used for scour simulations.	12
Figure 1.3. Definition sketch depicting the main flow features around a monopile. The "S" marks the separation line associated with the bed boundary layer. This figure is taken from Sumer and Fredsøe (2002).	16
Figure 1.4. Bed shear stress amplification along the symmetry line upstream of the pile. Comparison is with experimental data given by Roulund et al. (2005) and Hjorth (1975).	17
Figure 1.5. Magnitude of the bed shear stress amplification in the (a) model and (b) experiment of Hjorth (1975).	17
Figure 1.6. Simulated scour development where the time is indicated in minutes. The dimensionless scour depths can be read from the side panels.	18
Figure 1.7. Simulated scour depth time series at the (a) upstream and (b) downstream edge of the monopile. Scenario 1: full model results, Scenario 2: suspended sediment swiched off, Scenario 3: suspended sediment switched off and vortex shedding disabled.	19
Figure 1.8. Computed equilibrium scour profile along the line of longitudinal symmetry. Simulation scenarios are as described in the caption of Figure 1.7.	19
Figure 1.9. Sound-meter registration of the Indian Ocean tsunami on December 26, 2004 from the yacht Merdcator in the bay of Nai Ham, at the southwestern tip of Phuket, Thailand. The vertical axis measures depth in meters (from the keel i.e. 2 m below mean water level); The horizontal axis measures time in hours.	21
Figure 1.10. Comparison of two regression equations: (a) (1.31a) and (b) (1.31b) for predicting the time scale of scour, based on the experimental data set of Sumer et al. (1992).	23
Figure 1.11. Computed time series of (a) free stream velocity and (b) scour depth at the front and back face of the monopile. The horizontal dashed line in (b) represents the equilibrium scour depth estimated from (1.24).	26
Figure 1.12. Snapshots of the computed tsunami-induced scour at selected times. The colorbar refers to the dimensionless sea bed elevation h_b/D.	27
Figure 1.13. Computed bed profiles along the centerline y=0 at selected times when the flow is (a) rightward and (b) leftward; The times selected correspond to shown in Figure 1.12. Note that the vertical scale is grossly exaggerated.	28
Figure 1.14. Comparison of computed scour depths with those predicted by the practical model. The tsunami cases depict the maximum scour depth (at both front and back sides) that occur during 1, 2, and 3 successive wave cycles. Also shown is the steady current result from Section 1.4.	31
Figure 2.1. Marine aquaculture examples: (a) An offshore aquaculture plant in Gulluk Bay, Turkey, (b) Salmon pens off Vestmanna - Faroe Islands, Denmark, (c) An offshore aquaculture plant in Gulf of Mexico. [Photo Credit: (a) Ahmet Cevdet Yalciner, Sena Acar – METU, (b) Erik Christensen – Wikipedia, (c) Snapperfarm – NOAA Fisheries Southeast Regional Office]	35
Figure 2.2. (a) Global aquaculture production by country in million tonnes, 1950–2010, as reported by the FAO, (b) Global aquaculture production by country for 2010 (Based on data sourced from the FishStat database).	36
Figure 2.3. The 2010 Chile earthquake and tsunami: (a) fishing vessels hurled inland, (b) drift simulation of the aquaculture rafts, (c) damage of aquaculture rafts, and (d). [Photo Credit: (a) Mercator Media, 2015, (b)-(c)-(d) Otsuka et al., 2009.]	38
Figure 2.4. An example of a commercial oyster bed in Japan – many of the oyster beds	39

and other aquaculture facilities along Japan's Pacific coast suffered heavy damage from the GEJE tsunami. [Photo Credit: http://what-when-how.com/water-science/aquaculture-water-science/]	
Figure 2.5. Damage on Oyster farms at Yamada Bay, Japan by 2011 GEJE Tsunami (Yalciner et al, 2011).	40
Figure 2.6. (a) Wreckage of shellfish culture gear and boats in Miyagi, (b) Miyako Station, Fisheries Research Agency - before the tsunami, (c) after the tsunami. [Photo Credit: (a) Walsh and Hanafusa (2013), (b) Fisheries Research Agency of Japan, (c) ©2013 DigitalGlobe, Cnes/Spot Image, Map data ©2013 Google, ZENRIN]	40
Figure 2.7. Model of a longline being forced by surface waves (Stevens et al., 2008).	42
Figure 2.8. Definition sketch of anchor leg (Fredriksson et al., 2004).	43
Figure 2.9. Three dimensional nature of the mesh (Fredriksson et al., 2008).	45
Figure 3.1. Distribution of the ecosystems in Portugal.	49
Figure 3.2. Coastal ecosystem zones in Portugal: the marine especial protected zones (ZPEs).	50
Figure 3.3. Coastal ecosystem zones in Portugal: the marine sites of communitarian importance (SIC).	51
Figure 3.4. Ria Formosa ecosystem lagoon located in the coastal area of Algarve, South of Portugal.	52
Figure 3.5. Map of active tectonic structures in the SWIM region (from Duarte et al., 2010).	53
Figure 3.6. Impact of tsunami in the Ria Formosa lagoon caused by the MPF tsunamigenic scenario.	54
Figure 3.7. Maximum tsunami current velocities computed at the Ria Formosa lagoon considering the MPF tsunamigenic scenario.	55

List of tables:	**page**
Table 1.1. Comparison of resulting dimensional (above dashed line) and dimensionless (below dashed line) quantities at selected field and simulated model conditions, based on a diameter length scaling factor λ=50. Dimensionless quantities maintained at both scales are highlighted in bold. The equilibrium scour depth *S* below has been estimated from (1.24).	24
Table 2.1. Vulnerability of fisheries and aquaculture systems (FAO, 2014b).	37
Table 2.2. Damage on Japan fisheries sector caused by the Great East Japan Earthquake and Tsunami (World Bank, 2012).	39

ABBREVIATIONS AND ACRONYMS

CFD: Computational fluid dynamics
DTU: Technical University of Denmark
FAO: Food and Agriculture Organization of the United Nations
RANS: Reynolds-Averaged Navier-Stokes
SIC: Marine sites of communitarian importance
SWIM: Southwest Iberia Margin
ZPE: Marine especial protected zones

DEFINITIONS

None.

CHAPTER 1. TSUNAMI-INDUCED SCOUR AROUND MONOPILE WIND TURBINE FOUNDATIONS

1.1. Introduction

Tsunamis are long waves, typically having periods the order of minutes to hours, that are generated by sudden motions of the sea bed e.g. due to undersea earthquakes or landslides. When such waves approach and/or reach the shoreline, they are potentially catastrophic, as has been well-documented e.g. in the recent tsunami event that occurred in the Indian Ocean (2004), as well as in the Tohuku tsunami off the coast of Japan (2011). Damage from the recent 2011 Tohuku tsunami, in particular, has been detailed recently within the ASTARTE project by Aydin et al. (2014, ASTARTE Deliverable 5.3), including description of damage to coastal protection structures, ports, ships, wharfs, and cargo handling machines, among others.

While the run-up, inundation, and destructive potential of tsunami events has received considerable attention in the literature, the associated interaction with the sea bed i.e. boundary layer dynamics, induced sediment transport, and resultant sea bed morphology, has received relatively little specific attention. Such issues and processes are important, however, both in assessing potential larger scale deposition and erosion in affected coastal regions, as well as in understanding smaller scale erosion, such as tsunami-induced local scour around coastal and offshore structures (e.g. monopiles, piers, pipelines, and breakwaters), which can potentially contribute to their failure. Studies investigating tsunami-induced scouring around coastal and offshore structures in any context are few, but include e.g. Wilson et al. (2012), who studied sediment scour and deposition within harbors; Chen et al. (2013), who studied tsunami-induced scour at coastal roadways; and Bricker et al. (2012), who conducted a field study of scour depths measured on the landward side of seawalls and floodwalls, as well as beside a building foundation footing, from the 2011 Tohoku tsunami. Experimental investigations on the tsunami-induced scour specifically around monopiles are seemingly limited to that of Tonkin et al. (2003), who studied the scour promoted by incident solitary waves around a cylinder on a sloping beach, where the cylinder was mounted near the shoreline. These experiments were also simulated numerically using a nonlinear shallow water model by Pan and Huang (2012), with the intent of simulating tsunami-induced scour around bridge piers. As seen from the above, most of the works considering the general topic of tsunami-induced scour have only recently been published i.e. in the past few years. Hence, a detailed understanding of the underlying processes, as well as general structure vulnerability, is presently lacking. The present Chapter aims to further the understanding of tsunami-induced scour, by numerically investigating tsunami-induced flow and scour processes around a monopile structure, representative of those commonly utilized as offshore wind turbine foundations.

Offshore wind farms are becoming an increasingly important source of energy in Europe and throughout many parts of the world. As context, the locations of numerous wind farms throughout Europe are shown in Figure 1.1. As can be seen, at present, most of these are located in the North and Baltic Sea regions, as well as off the coasts of the United Kingdom and Ireland. As demand for decarbonized electricity increases, e.g. to combat expected global warming and other climate change effects in the coming decades, their use is expected to become much more widespread globally, including increased employment e.g. by Mediterranean (where such developments have already begun, as seen in Figure 1.1) and other tsunami-prone countries and regions. While the scour around monopiles due e.g. to waves and tidal currents has been extensively studied (see e.g. Sumer and Fredsøe 2002), the potential scour around offshore wind turbine foundations induced by tsunami attack has not been previously studied, either experimentally or numerically. To ensure proper design, it is therefore important that a detailed understanding of the potential tsunami-

induced scour around such structures be improved, which is initiated in the present work, the results of which are summarized in this Chapter.

Figure 1.1. Map showing the location of several wind farms within Europe.

This Chapter is organized as follows: The hydrodynamic and turbulence models utilized in the numerical CFD model are described in Section 1.2, which are coupled to the sediment transport and morphological models described in Section 1.3. The fully-coupled numerical model is validated for flow and scour around a monopile in steady current conditions in Section 1.4. A methodology for assessing hydrodynamic and morphological similarity between field and (laboratory) model scales is presented in Section 1.5, which forms the basis for the numerical simulation of tsunami-induced scour around a monopile presented in Section 1.6. A simple methodology for predicting tsunami-induced scour in engineering practice is presented in Section 1.7, which is then reconciled with the numerical simulation results, both for transient tsunami waves as well as at the steady current limit. Conclusions are finally drawn in Section 1.8.

1.2. Hydrodynamic and turbulence model description

In this section, a description of the computational model used throughout the present Chapter is provided. The numerical model solves the incompressible Reynolds-averaged Navier–Stokes (RANS) equations:

$$\frac{\partial u_i}{\partial t} + u_j \frac{\partial u_i}{\partial x_j} = -\frac{1}{\rho}\frac{\partial p}{\partial x_i} + \frac{\partial}{\partial x_j}\left[2\nu S_{ij} + \frac{\tau_{ij}}{\rho}\right], \tag{1.1}$$

where the mean strain-rate tensor is

$$S_{ij} = \frac{1}{2}\left(\frac{\partial u_i}{\partial x_j} + \frac{\partial u_j}{\partial x_i}\right). \tag{1.2}$$

These are combined with the local continuity equation

$$\frac{\partial u_i}{\partial x_i} = 0\,. \tag{1.3}$$

Here, u_i are the mean (phase-resolved) velocities, x_i are the Cartesian coordinates, t is time, p is the pressure, ν is the fluid kinematic viscosity, ρ is the fluid density, and τ_{ij} is the Reynolds stress tensor, which accounts for additional (normal and shear) stresses due to momentum transfer from turbulent fluctuations u'_i. Throughout the present Chapter, the Reynolds stress tensor will be defined according to the constitutive relation

$$\frac{\tau_{ij}}{\rho} = -\overline{u'_i u'_j} = 2\nu_T S_{ij} - \frac{2}{3}k\delta_{ij}\,, \tag{1.4}$$

where δ_{ij} is the Kronecker delta, ν_T is the eddy viscosity,

$$k = \frac{1}{2}\overline{u'_i u'_i} \tag{1.5}$$

is the turbulent kinetic energy density, and the overbar denotes time averaging (or ensemble averaging in unsteady flows). To achieve closure, the two-equation k-ω turbulence model of Wilcox (2006) is adopted. In this model, the eddy viscosity is defined by

$$\nu_T = \frac{k}{\tilde{\omega}}, \quad \tilde{\omega} = \max\left\{\omega, C_{\lim}\sqrt{\frac{2S_{ij}S_{ij}}{\beta^*}}\right\}, \tag{1.6}$$

which incorporates a stress-limiting feature, with $C_{\lim}$=7/8. This model additionally uses transport equations for the turbulent kinetic energy density k

$$\frac{\partial k}{\partial t} + u_j\frac{\partial k}{\partial x_j} = \frac{\tau_{ij}}{\rho}\frac{\partial u_i}{\partial x_j} - \beta^* k\omega + \frac{\partial}{\partial x_j}\left[\left(\nu + \sigma^*\frac{k}{\omega}\right)\frac{\partial k}{\partial x_j}\right], \tag{1.7}$$

as well as for the specific dissipation rate ω

$$\frac{\partial \omega}{\partial t} + u_j\frac{\partial \omega}{\partial x_j} = \alpha\frac{\omega}{k}\frac{\tau_{ij}}{\rho}\frac{\partial u_i}{\partial x_j} - \beta\omega^2 + \frac{\sigma_d}{\omega}\frac{\partial k}{\partial x_j}\frac{\partial \omega}{\partial x_j} + \frac{\partial}{\partial x_j}\left[\left(\nu + \sigma\frac{k}{\omega}\right)\frac{\partial \omega}{\partial x_j}\right], \tag{1.8}$$

where

$$\sigma_d = H\left\{\frac{\partial k}{\partial x_j}\frac{\partial \omega}{\partial x_j}\right\}\sigma_{do}, \tag{1.9}$$

and $H\{\cdot\}$ is the Heaviside step function, taking a value of zero when the argument is negative and a value of unity otherwise. The standard model closure coefficients are used: α=13/25, β^*=9/100, σ=1/2, σ^*=3/5, and σ_{do}=1/8, $\beta=\beta_0 f_\beta$ and β_0=0.0708, with

$$f_\beta = \frac{1+85\chi_\omega}{1+100\chi_\omega}, \quad \chi_\omega = \left|\frac{\Omega_{ij}\Omega_{jk}S_{ki}}{\left(\beta^*\omega\right)^3}\right|, \quad \Omega_{ij} = \frac{1}{2}\left(\frac{\partial u_i}{\partial x_j} - \frac{\partial u_j}{\partial x_i}\right). \tag{1.10}$$

The hydrodynamic model described above is subject to the following boundary conditions. At friction wall boundaries, a no-slip condition is imposed whereby velocities are set to zero. Alternatively, Neumann conditions are applied to the three components of the velocity and scalar hydrodynamic quantities at the top symmetry boundary, which is in line with the approach in Roulund et al. (2005). Slip wall conditions are applied at side wall boundaries. Flow is driven by specifying velocity and turbulence quantities at the left hand (inlet) boundary. This will be described in more detail on a case-by-case basis in what follows. At the opposite right-hand (outlet) boundary, zero-gradient boundary conditions are imposed for all quantities except the pressure term, p, which is set to a reference zero value at the outlet boundary.

At the bottom (sea bed) boundary, as well as the monopile cylinder, a generalized wall function approach developed recently by Fuhrman et al. (2014) is used. Under this approach, the friction velocity U_f is determined from the tangential velocity at the nearest cell center, based on the profile of Cebeci and Chang (1978)

$$\frac{u}{U_f} = 2\int_0^{y_c^+} \frac{dy^+}{1+\left[1+4\kappa^2\left(y^+ + \Delta y_{cc}^+\right)^2 C\right]^{1/2}}, \tag{1.11}$$

$$C = \left[1-\exp\left(-\frac{\left(y^+ + \Delta y_{cc}^+\right)}{25}\right)\right]^2, \tag{1.12}$$

$$\Delta y_{cc}^+ = 0.9\left[\sqrt{k_s^+} - k_s^+\exp\left(-\frac{k_s^+}{6}\right)\right], \tag{1.13}$$

who generalized the van Driest (1956) velocity profile to incorporate potential roughness effects. Here, $y_c=\Delta y/2$ is the normal distance from the wall to the first cell center, expressed in terms of wall coordinates as $y^+_c=y_cU_f/\nu$, Δy is the near-wall cell thickness, κ=0.4 is the von Karman constant, and k_s is Nikuradse's equivalent sand grain roughness. At the bed k_s=2.5d is used, with d the sediment grain size, whereas at the cylinder k_s is kept sufficiently small ($k_s=10^{-5}$ m) such that it is effectively modelled as hydraulically smooth. The friction velocity is then used within the generalized wall functions for k and ω in the cells nearest to the wall, according to

$$\frac{k}{U_f^2} = \min\left\{A\Delta y^{+2}, \frac{1}{\sqrt{\beta^*}}\right\} \tag{1.14}$$

and

$$\frac{\omega \nu}{U_f^2} = \max\left\{ \frac{B}{\Delta y^{+2}}, \frac{1}{\sqrt{\beta^*}\kappa \Delta y^+} \right\}. \tag{1.15}$$

The first arguments in these functions ensure that these variables follow their proper scaling $k \sim y^2$ and $\omega \sim 1/y^2$ for near-wall cells within the viscous sub-layer (see e.g. Wilcox 2006). The values $A=1/(\delta^{+2}\beta^{*1/2})=0.02466$ and $B=\delta+/(\beta^{*1/2}\kappa)=96.885$ are used, which ensure a continuous transition to the (fully turbulent) second arguments at $\Delta y^+ = \delta^+$, where $\delta^+=11.626$ is taken as the viscous sub-layer thickness (in dimensionless wall coordinates).

The computational domain is discretized into finite volumes of quadrilateral blocks in varying shapes and dimensions. Figure 1.2 shows the boundaries of the domain on an example computational mesh typical of that used for the forthcoming scour calculations. The calculation domain utilized in the present Chapter has the following dimensions: length, l=20D, width, w=15D, and height, h=2D, in which D is the monopile diameter. The total number of cells comprising the computational domains utilized is $O(10^5)$. The monopile is located at the center of the domain $(x,y)=(0,0)$. As an indication of computational expense, a fully coupled hydrodynamic and morphological calculation lasting 1 min of physical time for the three dimensional scour around a vertical pile problem requires approximately 10 full days of CPU time, when simulated in parallel on eight modern processors. It is emphasized that considerable effort has been put into optimizing the computational mesh for the best grid and time convergence.

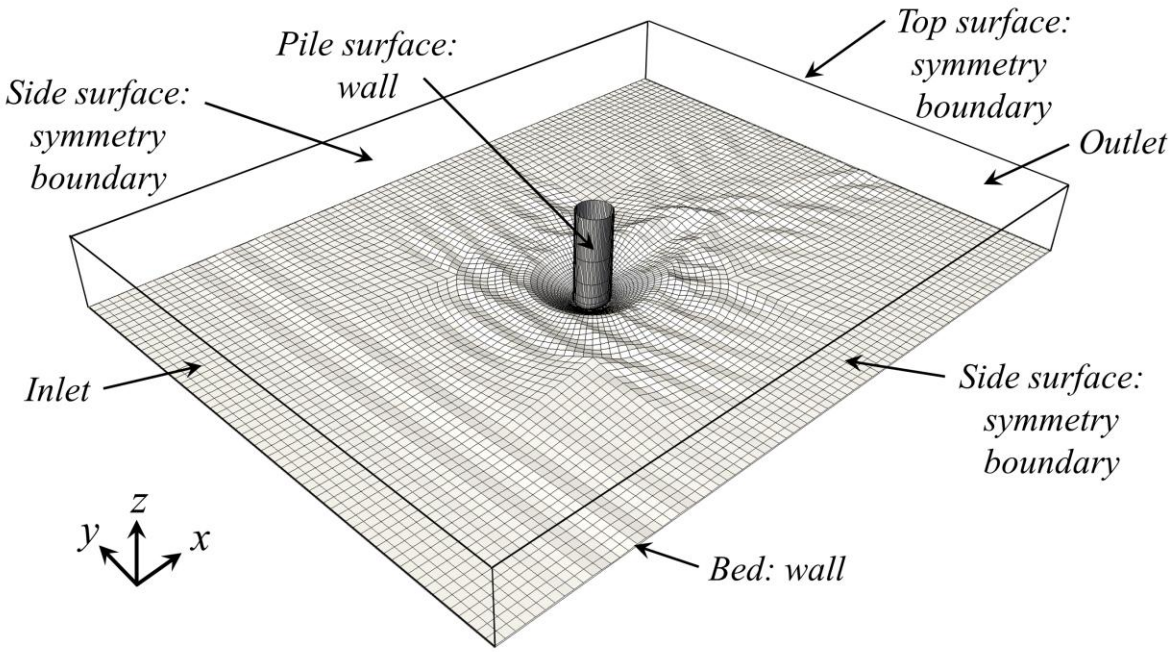

Figure 1.2. Example computational domain and boundaries used for scour simulations.

1.3. Sediment transport and morphological model description

The present subsection will describe the sediment transport and morphological models, which are coupled to the hydrodynamic and turbulence closure models described above. The model makes use of separate bed and suspended sediment load descriptions. The rate of bed load sediment transport q_B is calculated based on the well-known method described in detail by Engelund and Fredsoe (1982), as well as Roulund et al. (2005) who generalized the well-known transport formulation of Engelund and Fredsoe (1976) to account for three-dimensional effects as well as bed-slope modifications. For brevity, this model will not be described herein.

The suspended sediment model is, alternatively, based on a turbulent-diffusion equation (e.g. Fredsøe and Deigaard 1992, p. 238) of the form

$$\frac{\partial c}{\partial t} + \left(u_j - w_s \delta_{j3}\right)\frac{\partial c}{\partial x_j} = \frac{\partial}{\partial x_j}\left[\left(\nu + \nu_T\right)\frac{\partial c}{\partial x_j}\right], \tag{1.16}$$

where c is the suspended sediment concentration, and w_s is the settling velocity of sediment grains. The settling velocity is solved for a given grain diameter d using the drag-coefficient approach described in Fredsøe and Deigaard (1992). Equation (1.16) is solved on a sub-set of the main computational mesh, i.e. where near-bed cells below a so-called reference level b are removed, as described in detail by Jacobsen et al. (2014, see their Figure 2). At all boundaries except for the bottom, a zero-flux condition for c is used. At the erodible bottom boundary a so-called reference concentration boundary condition is imposed. More specifically, the method of Engelund and Fredsoe (1976) is used, with the concentration at the reference level set to

$$c_b(\theta) = \frac{c_0}{\left(1 + 1/\lambda_b\right)^3}, \tag{1.17}$$

where c_0=0.6, and the linear concentration λ_b is

$$\lambda_b^2 = \frac{\kappa^2 \alpha_1^2}{0.013 s\theta}\left(\theta - \theta_c - \frac{\pi}{6}\mu_d p_{EF}\right), \tag{1.18}$$

where

$$p_{EF} = \left[1 + \left(\frac{\pi \mu_d}{6(\theta - \theta_c)}\right)^4\right]^{-1/4} \tag{1.19}$$

is the probability of moving grains, and

$$\theta = \frac{\tau_0}{\rho g (s-1) d} = \frac{U_f^2}{(s-1) g d} \tag{1.20}$$

is the Shields parameter, in which $\tau_0 = \rho U_f^2$ is the wall shear stress, s is the relative density of the sediment grains (taken as s=2.65, unless otherwise noted), and g=9.81 m/s^2 is the gravitational acceleration. Throughout the present work, the coefficient of dynamic friction is set to μ_d=0.51. The critical Shields parameter θ_c is computed from a base value θ_{c0}=0.05, adjusting for bed-slope effects

as described in Roulund et al. (2005). Following Fuhrman et al. (2014), throughout the present work, the reference level is taken as b=3.5d. To prevent un-physical 'overloading' conditions (i.e. where reference c_b is forced to be smaller than the concentration immediately above) from occurring in the model, the solution suggested by Justesen et al. (1986) is finally invoked. That is, if the concentration close to the bed exceeds the reference concentration $c_b(\theta)$ the value in practice is taken from the cell adjacent to the boundary.

The morphology of the bed elevation h_b is based on the sediment continuity (Exner) equation

$$\frac{\partial h_b}{\partial t} = \frac{1}{1-n}\left[-\frac{\partial q_{Bi}}{\partial x_i} + D + E\right], \quad i = 1, 2 \tag{1.21}$$

where n=0.4 is the bed porosity, and D and E are the deposition and erosion stemming from the suspended sediment model. These are, respectively, calculated according to

$$D = (w_s - u_3)c_b\,, \tag{1.22}$$

$$E = (\nu + \nu_T)\left.\frac{\partial c}{\partial x_3}\right|_{x_3=b}\,. \tag{1.23}$$

It is stressed that the simulated bed morphology within the present work is continuous, always being based on the instantaneous sediment transport fields, i.e. the model does not make use of morphological rates averaged over a period or any other time scale. Accordingly, morphological and hydrodynamic times are equivalent. The temporal integration of (1.21) is herein based on the explicit Euler method. For more specific details regarding the numerical evaluation of the three terms within the right-hand side of (1.21), the interested reader is referred to Jacobsen et al. (2014). It is finally noted that, to prevent excessive erosion induced by the imposed uniform flow at the boundary, the sea bed is fixed at the left (inlet) boundary and relaxed to full morphology over a distance spanning a few pile diameters.

Experience has shown that, if left unchecked, the morphological model can lead to local bed slopes in excess of the angle of repose. To combat such un-physical steepening, the physically based sand slide model described in detail by Roulund et al. (2005) is implemented. In the present work, this sand slide model is activated at positions where the local bed angle exceeds the angle of repose ϕ_s=32° and is de-activated once the local bed angle is reduced to 30°. Additionally, some local filtering of the bed is necessary in the scour runs for stability reasons. For this purpose, a filtering algorithm based on the least-squares method is applied to the morphological rates in the near vicinity of the pile to smooth out small-sized (i.e. high wavenumber) ripples that can occur inside the scour hole adjacent to the pile, where the numerical stability of the mesh motion computations becomes critical due to increased rates of change in bed elevations. The strength of filtering inside and around the scour hole is kept variable with the use of a hyperbolic function, based on the radial distance from the origin of the domain, as described by Baykal et al. (2015). This results in the filtering of small-sized ripples inside the scour hole, while still allowing resolution of any far-field bed ripples that develop.

The equations constituting the fully coupled model outlined above are solved numerically using the open-source CFD toolbox OpenFOAM, v. 1.6-ext, making use of a finite volume spatial discretization with a collocated variable arrangement, in conjunction with a standard PIMPLE algorithm. Again, for further details see Jacobsen et al. (2014).

1.4. Model validation

In this section, the numerical model described above will be validated for flow features and scour around a vertical cylindrical pile mounted on a horizontal plane soil bed, subjected to a steady current. Given the generally long periods (spanning several minutes to hours) typical of tsunamis, validation based on steady current flows can be considered more relevant than e.g. based on experiments using typical wind wave scales. Given the large computational costs of advanced CFD models such as those utilized in the present Chapter, simulations are necessarily limited to model spatial and temporal scales. The validation presented here is part of a wider study of Baykal et al. (2015), who performed an extensive numerical investigation of flow and scour around a vertical circular cylinder.

For the present purposes we will consider specifically a case having a monopile diameter D=0.04 m mounted on an initially flat bed. Simulations will utilize a computational domain having height h=2D=0.08 m, with bed sediment grain size d=0.17 mm i.e. corresponding to fine sand. Note that under steady current conditions, the boundary layer thickness can be taken as identical to the domain height i.e. $\delta=h$.

Prior to simulating this case in full, the model has first been run with the monopile removed, with the flow driven by a constant horizontal pressure gradient (i.e. a body force), such that uniform flow conditions develop across the domain with friction velocity U_f=0.019 m/s and with a mean (depth averaged) flow velocity U=0.413 m/s. In terms of dimensionless quantities, these flow conditions correspond to a Reynolds number $Re_D=UD/\nu=3.3\times10^4$ and a Shields parameter θ=0.13 i.e. these conditions can be taken as in the live-bed scour regime. The resulting vertical profiles for the horizontal velocity u, turbulent kinetic energy k, and the specific dissipation rate ω, in these uniform flow conditions are then set as the inlet boundary conditions (see again Figure 1.2) for subsequent simulations with the monopile placed such that it is centered at the origin.

In what follows, the model will be tested both on a fixed rigid bed (achieved by switching off the morphological model), as well as on a live bed, where the fully-coupled hydrodynamic and morphodynamic model described previously is utilized in its entirety. We will begin our investigation by considering the flow properties of a steady current flow on a fixed rigid bed. Special attention will be paid to the bed shear stresses that develop, as these are the primary driving factor for the resultant sediment transport and scour processes. It is additionally emphasized that results for the lee wake flow have also been systematically validated in Baykal et al. (2015).

The main flow features around a vertical cylindrical pile exposed to a steady current on a plane bed are the horseshoe vortex formed in front of the pile, the lee-side vortices (usually in the form of vortex shedding), contracted streamlines around the sides of the pile, and the down-flow in front of the pile due to deceleration of the flow. These features are illustrated in the definition sketch provided in Figure 1.3. The horseshoe vortex in front of the pile is an end result of the adverse pressure gradient on the bed upstream of the pile, which is actually induced by the presence of the pile in a steady current. This adverse pressure gradient enforces a three-dimensional boundary layer separation just in front of the pile and results in a vortical structure surrounding the upstream perimeter of the pile and fading away downstream. The size of the horseshoe vortex in front of a circular pile with a smooth bed depends mainly on the ratio of the bed-boundary-layer thickness to the pile diameter δ/D (Baker 1979), with additional dependence on the pile Reynolds number Re_D

=UD/ν, where U is the free-stream velocity, and the ratio of bed roughness to pile diameter k_s/D in the case of rough beds.

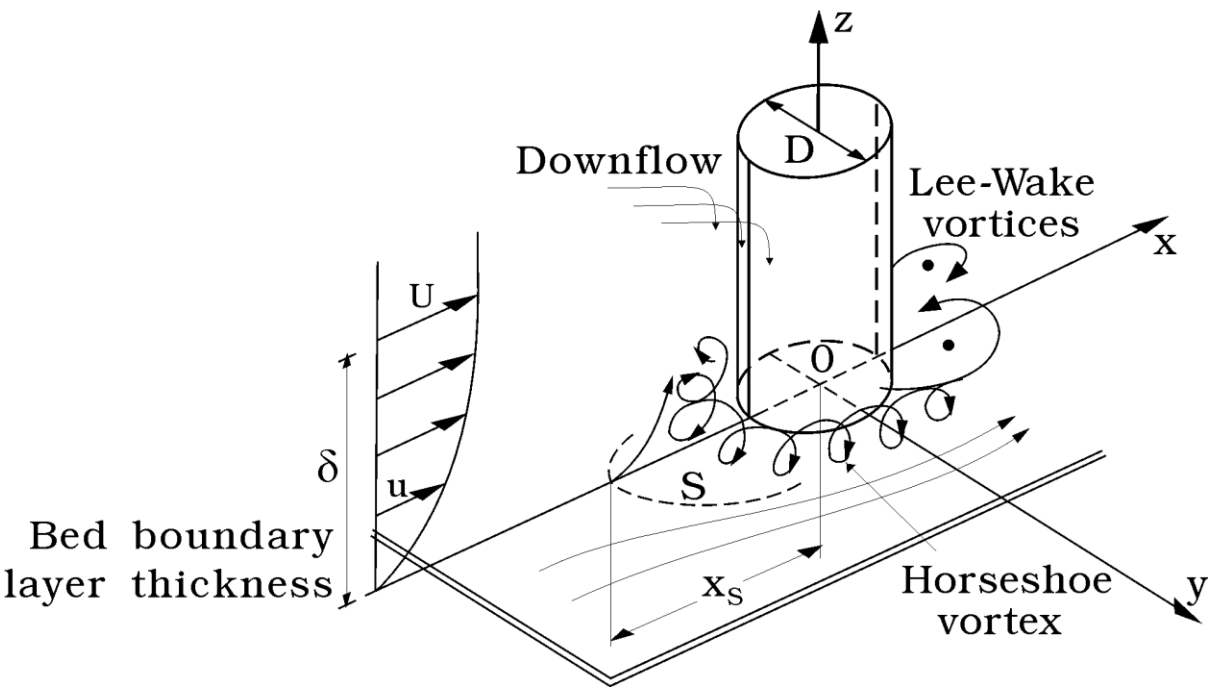

Figure 1.3. Definition sketch depicting the main flow features around a monopile. The "S" marks the separation line associated with the bed boundary layer. This figure is taken from Sumer and Fredsøe (2002).

As a first means of validation, Figure 1.4 presents the computed amplification of the bed shear stress relative to the far field along the x-axis (upstream of the monopile i.e. where the horseshoe vortex is present). For the sake of comparison, the amplifications measured in previous smooth bed experiments by Roulund et al. (2005) and Hjorth (1975) (see his Figure 6.18b, p. 133, as well as the Test-1 data in Figure 16, p. 376 of Roulund et al. 2005) are likewise depicted. Here, the amplification of the bed shear stress is defined as τ_0/τ_∞, in which τ_0 is the bed shear stress and τ_∞ is the undisturbed (far field) bed shear stress. The negative bed shear stress region corresponds to the location of the horseshoe vortex in front of the pile. Figure 1.4 shows that the numerical and experimental results generally agree well outside the horseshoe vortex for $x/D<-1.2$. However, for $-1.2<x/D<-0.5$, the bed shear stress is slightly under-predicted by the numerical model with respect to the data given by Hjorth (1975), with the maximum difference between the model and the experiment being around 30%. This is considered acceptable, and is also consistent with the findings given in Roulund et al. (2005). No explanation was provided by Roulund et al. (2005) for this difference, though one will be offered in the next paragraph. Most importantly in terms of simulating the scour process, this result confirms the ability of the present model to reasonably capture the horseshoe vortex in front of the monopile, which is the predominant flow feature in the near vicinity of the monopile.

As further validation of the induced bed shear stresses in the near vicinity of the monopile, Figure 1.5 compares the amplification of the bed shear stress, defined as the ratio of the magnitude of the bed shear stress vector to the value of the undisturbed bed shear stress ($|\tau_0/\tau_\infty|$), obtained from the present model with those from Hjorth's (1975) experiments (see his Figure 6.18b, p. 133). The present calculations and the measurements are seen to be in generally good agreement in terms of the magnitude of the bed shear stresses around the cylinder. However, the radial location of the

maximum bed shear stress is found to be slightly different from the measurements. This minor discrepancy likely explains the previously discussed difference between the model and measurements shown in Figure 1.4.

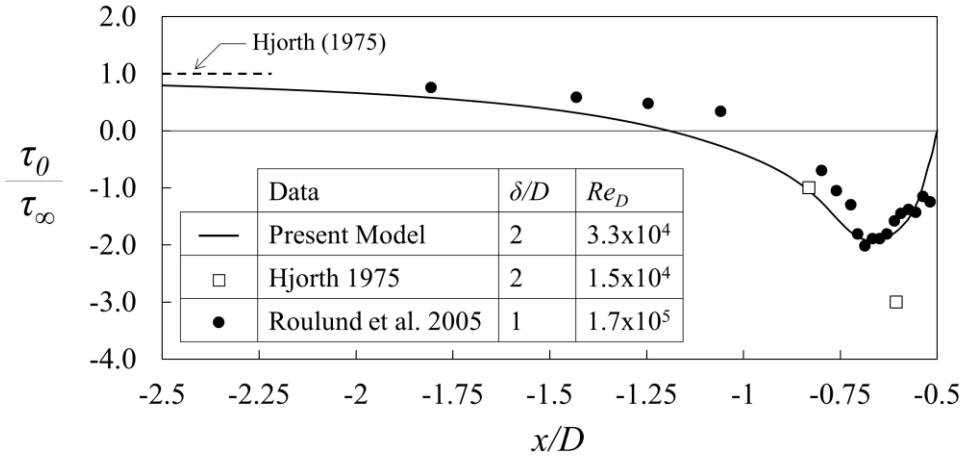

Figure 1.4. Bed shear stress amplification along the symmetry line upstream of the pile. Comparison is with experimental data given by Roulund et al. (2005) and Hjorth (1975).

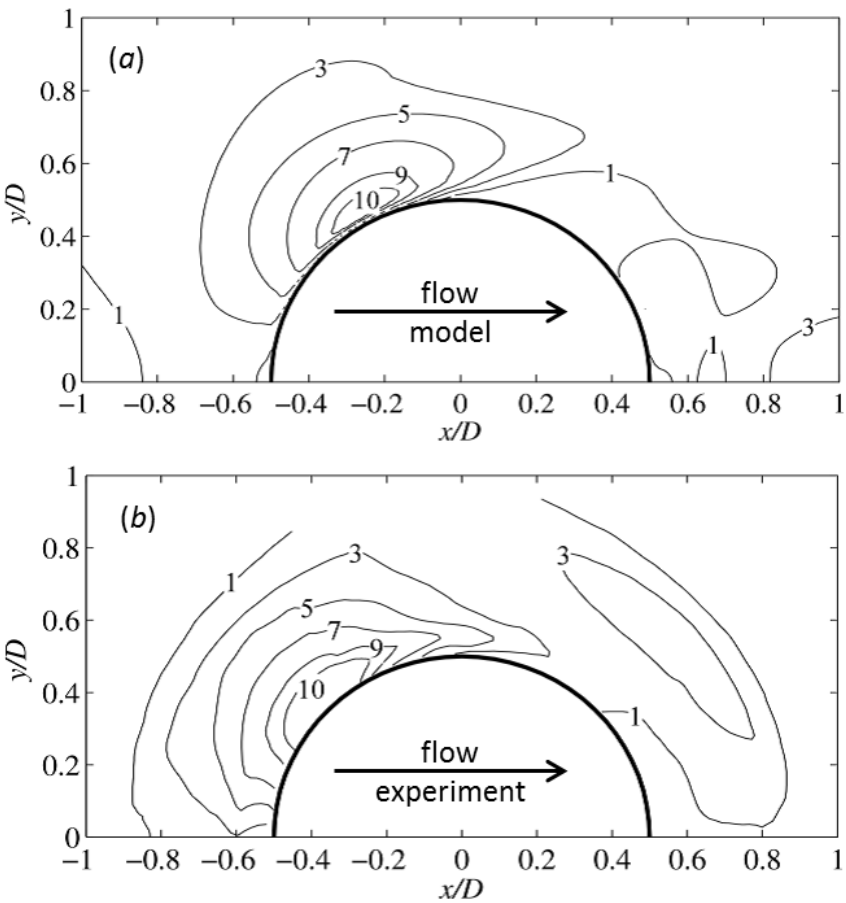

Figure 1.5. Magnitude of the bed shear stress amplification in the (a) model and (b) experiment of Hjorth (1975).

Having demonstrated the model's ability to reasonably produce the bed shear stress field utilizing rigid bed simulations, we will now focus on simulation of the induced scour process i.e. with sediment transport and morphological models now switched on. Scour around a vertical pile structure has been previously investigated in detail by Roulund et al. (2005), where steady-state flow calculations around a vertical pile over an initially plane bed were incorporated within a morphology model based on bed load sediment transport and sand slide processes only. In the present study, the additional effects of unsteady flow structures and suspended sediment transport will additionally be incorporated.

Figure 1.6 shows a sequence of pictures illustrating the time evolution of the simulated scour hole driven by the present steady current conditions. In the figure, one can see (i) the semi-circular shape (in plan view) of the upstream part of the scour hole with a slope equal to the angle of repose, (ii) the formation of a 'bar' downstream of the monopile (the deposited sand), and its downstream migration, (iii) the formation of a gentler slope of the downstream side of the scour hole, (iv) the formation and migration of bed ripples at the downstream side of the scour hole, and, finally (v) the bed material eroded and piled up along the edges of the scour hole downstream. These are caused by counter-rotating streamwise phase-averaged lee-wake vortices close to the bottom, as discussed in detail by Baykal et al. (2015, see their Figure 12*a*).

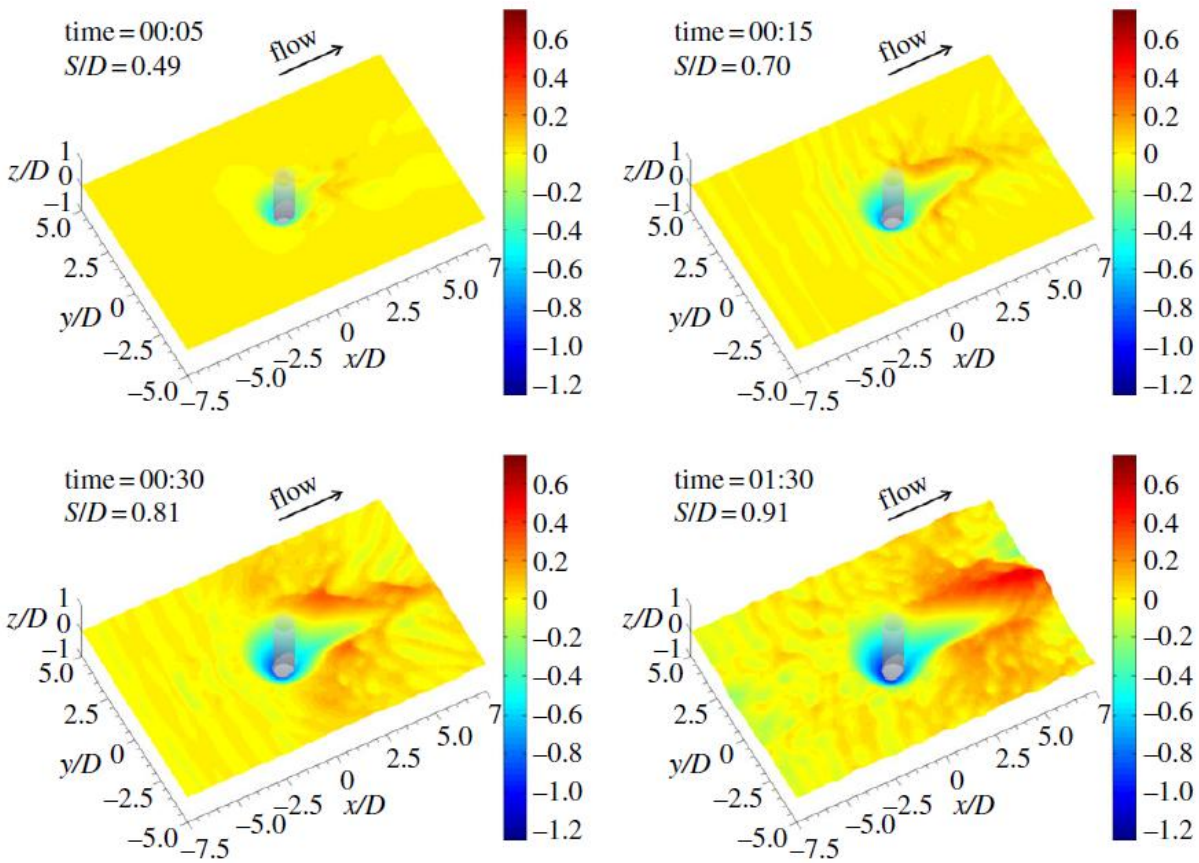

Figure 1.6. Simulated scour development where the time is indicated in minutes. The dimensionless scour depths can be read from the side panels.

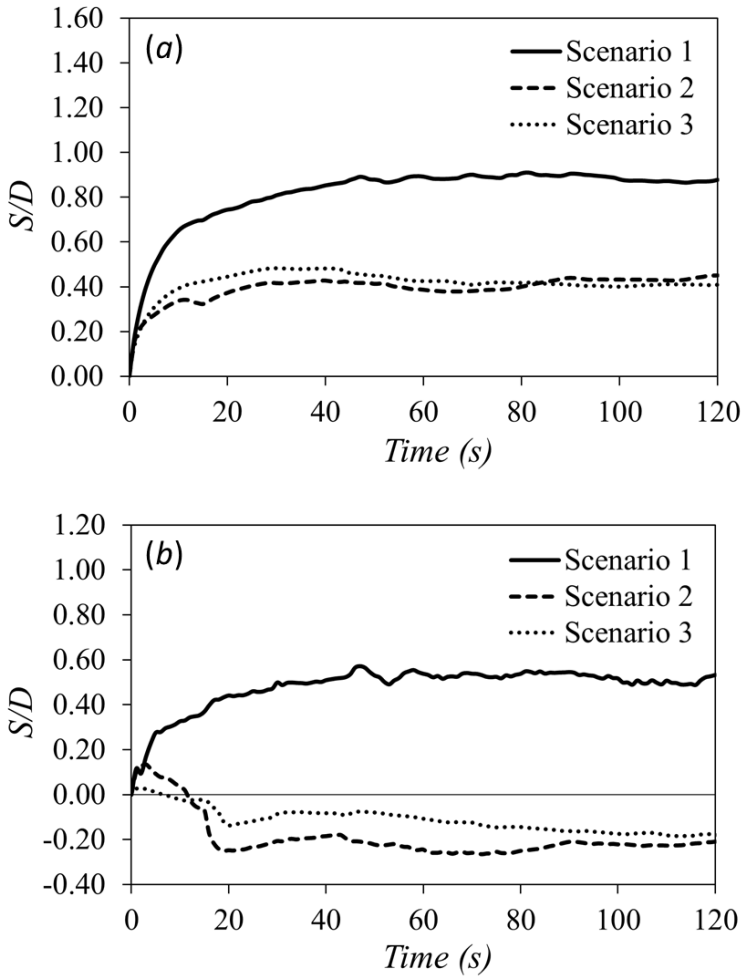

Figure 1.7. Simulated scour depth time series at the (a) upstream and (b) downstream edge of the monopile. Scenario 1: full model results, Scenario 2: suspended sediment switched off, Scenario 3: suspended sediment switched off and vortex shedding disabled.

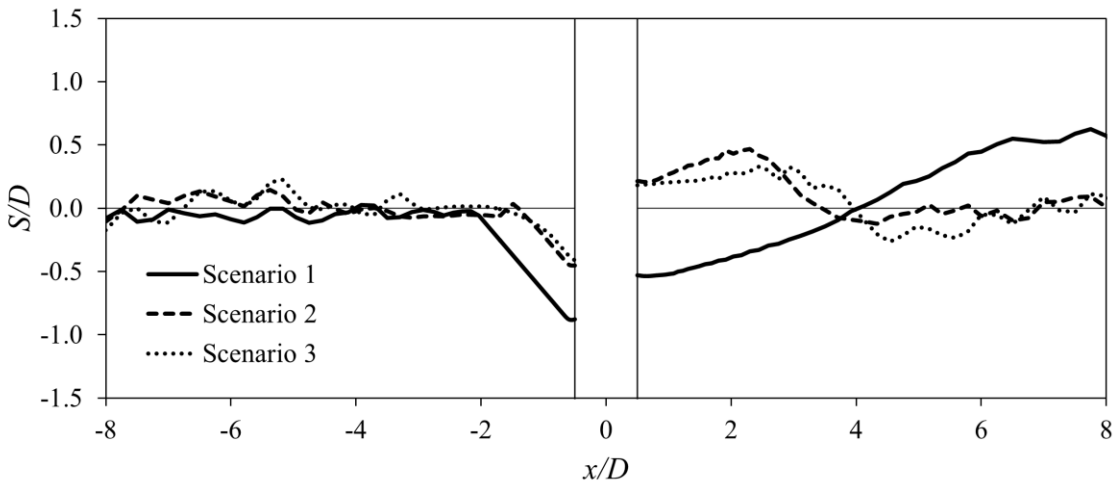

Figure 1.8. Computed equilibrium scour profile along the line of longitudinal symmetry. Simulation scenarios are as described in the caption of Figure 1.7.

Figure 1.7 (full lines) shows the time development of the computed scour depth at the upstream side (Figure 1.7*a*) and at the downstream side (Figure 1.7*b*) of the pile. Figure 1.8 similarly shows the computed scour-hole profiles along the upstream–downstream symmetry line, after a simulated scour time corresponding to t=2 min i.e. after equilibrium scour has been reached. In addition to the full model results (full lines, dubbed "Scenario 1"), results are also depicted in these figures from otherwise identical simulations, but with the suspended sediment model switched off (dashed lines, dubbed "Scenerio 2"), as well as with vortex shedding additionally disabled (dotted lines, dubbed "Scenerio 3", achieved by changing numerical schemes, as described in detail in Baykal et al. 2015). As can be seen from comparison of Scenario 1 and 2, significant differences (both up and downstream of the monopile) are apparent when a bed load-only model is utilized, whereas effects of vortex shedding appear to be of lesser importance in the simulation of the scour process. Without a suspended model, sediment cannot be picked up and carried downstream by the flow, leading to accretion rather than scour on the lee side of the monopile.

Turning our attention back to the full model results (full lines in Figures 1.7 and 1.8), the equilibrium scour depth is seen to be approximately S/D=0.91, where S is the scour depth in front of the pile. As validation, this value may be compared with the experimentally-based expression of Sumer and Fredsøe (2002, their eq. (3.11), p. 181):

$$\frac{S}{S_0} = 1 - \exp\left(-0.55\frac{\delta}{D}\right). \tag{1.24}$$

Invoking δ/D=2 for the present case, and taking S_0/D=1.3 as the widely-accepted equilibrium current-induced scour value on a circular pile (without depth limitation), this yields a target scour depth corresponding to S/D=0.87 i.e. in remarkably good agreement with the computed value.

Based on the above simulations, the present CFD model has demonstrated the ability to (reasonably) accurately predict the current-induced flow, bed shear stresses, as well as scour process around a monopile. For further details regarding the results presented in the present section the interested reader is again referred to the recent work of Baykal et al. (2015). Additionally, as yet further validation in a separate, but related context, it is also noted that the fully-coupled (hydrodynamic and morphologic) model described in the present Chapter has likewise been validated and utilized to simulate wave-induced scour and backfilling processes beneath submarine pipelines by Fuhrman et al. (2014). Links to both of these papers, which acknowledge ASTARTE support, can be found on the ASTARTE website.

1.5. Similarity of tsunami field and model scales

As noted in the previous section, due to the large computational expenses associated with advanced CFD models, it is presently only feasible to simulate such scour processes around a monopile at model (laboratory) spatial and temporal scales. Therefore, prior to conducting such numerical simulations involving tsunami-induced scour, it is necessary to first establish a methodology for maintaining similarity of model and full field scales, in terms of properly chosen dimensionless quantities. In this section such a methodology for establishing hydrodynamic and morphodynamic similarity within an unsteady tsunami-induced scouring process will be introduced and described. This methodology will then be utilized to determine parameters used for numerical simulation at model scales in the subsequent section.

As inspiration for obtaining typical full tsunami scales, we will now consider a well-known measurement of the 2004 Indian Ocean tsunami event from the yacht Mercator, taken at a water depth h=14 m, which is depicted in Figure 1.9. Based on this signal, Madsen and Fuhrman (2008) estimated that the leading wave of this tsunami could be reasonably represented as sinusoidal, with a wave period T=13 min and surface elevation amplitude A=2.5 m. Based on these parameters, the velocity magnitude U_m beneath such an event can be readily estimated, as a first approximation, based on linear shallow water theory

$$U_m = A\sqrt{\frac{g}{h}} \ , \tag{1.25}$$

yielding U_m=2.1 m/s. It can be noted that a sinusoidal description for this tsunami event can be considered a much closer approximation than would e.g. a signal based on a solitary wave description, which would only include positive surface displacement, and which would not allow for the effective period and wave amplitude to be determined independently (see e.g. the discussion of Madsen et al. 2008). Note also that, based on records of free surface fluctuations at several locations during the 2011 Japan Tohoku tsunami, Chan and Liu (2012) have likewise concluded that the leading tsunami waves, in both near-field and far field regions, can be characterized as small amplitude long waves i.e. consistent with the linear shallow water description utilized above. The previously mentioned velocity magnitude U_m and period T will be utilized in what follows as characteristic values, representative of tsunamis at full scale, though obviously precise values may differ from these for other specific events and/or locations. Note that the corresponding water depth (h=14 m) for this signal is conveniently appropriate for the present considerations, as monopile foundations are commonly utilized within offshore wind turbines out to depths no larger than about 30 m. Additionally, for the purposes of our discussion, a full-scale monopile diameter of D=5 m will be considered, which is typical for offshore wind turbine foundations. Finally, for the sake of our discussion, bed sediments at full scale will be considered to have a typical grain size d=0.30 mm i.e. corresponding to medium-fine sand.

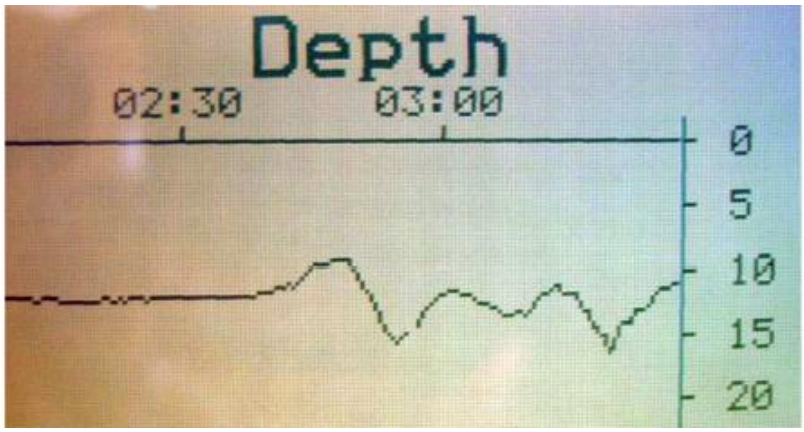

Figure 1.9. Sound-meter registration of the Indian Ocean tsunami on December 26, 2004 from the yacht Mercator in the bay of Nai Ham, at the southwestern tip of Phuket, Thailand. The vertical axis measures depth in meters (from the keel i.e. 2 m below mean water level); The horizontal axis measures time in hours.

Based on the values above, the following important hydrodynamic quantities can be estimated using widely-utilized dimensionally-correct expressions from the literature. The wave boundary layer

thickness δ can be estimated based e.g. on the well-known expression of Fredsøe and Deigaard (1992):

$$\frac{\delta}{D} = \frac{k_s}{D} 0.09 \left(\frac{a}{k_s} \right)^{-0.18}, \quad a = \frac{U_m T}{2\pi}. \tag{1.26}$$

This yields the estimate δ=2.36 m for the parameters considered, a value which has additionally been confirmed from pure boundary layer simulations, based on the one-dimension vertical turbulent boundary layer model of Fuhrman et al. (2013). Notice that, though expectedly much larger than typical wind wave boundary layer thicknesses of say *O*(10 cm), the estimated boundary layer thickness is still only a fraction of the water depth, *h*=14 m, in this example. The depth-based Froude number $Fr_h=U_m/(gh)^{0.5}$=0.18 is also relatively small (<0.2). Hence, for the conditions considered, the effects associated with the physical water depth *h* can be considered small, with associated length scales then based entirely on the monopile diameter *D*. Accordingly, we define a dimensionless Froude number as follows:

$$Fr_D = \frac{U_m}{\sqrt{gD}}. \tag{1.27}$$

Also of interest, is the so-called Keulegan-Carpenter number

$$KC = \frac{U_m T}{D}, \tag{1.28}$$

which governs the formation and relative extension of the wake pattern in oscillatory motion.

In addition to describing the wave parameters, it is likewise of interest to estimate the time scale of the expected scour process. Under both current and wave conditions, this is widely known to depend on the Shields parameter, which is proportional to the ratio of driving and stabilizing forces on sediment grains. This can be defined as

$$\theta_m = \frac{U_{fm}^2}{(s-1)gd}, \tag{1.29}$$

where the maximum value of the friction velocity U_{fm} can be estimated from

$$U_{fm} = \sqrt{\frac{f_w}{2}} U_m, \quad f_w = \exp\left\{ 5.5 \left(\frac{a}{k_s} \right)^{-0.16} - 6.7 \right\}, \tag{1.30}$$

which utilizes the rough-bed wave friction factor f_w expression from Fuhrman et al. (2013).

The time scale of scour T_s, representing the time required for significant scouring to occur, can now be estimated. Due to the long durations typical of tsunamis, this time scale will be based on existing steady current scour research, but invoking the expected tsunami-induced wave boundary layer thickness from (1.26). Hence, both current-like and wave-like features of tsunami-induced flows will be accounted for. Based on a series of steady current scour experiments, Sumer et al. (1992) proposed the following regression equation for estimating the scour time scale:

$$T_s^* = T_s \frac{\sqrt{g(s-1)d^3}}{D^2} = \frac{1}{2000}\frac{\delta}{D}\theta_m^{-2.2} \tag{1.31a}$$

It is important to emphasize, however, that (1.31*a*) is based on experiments spanning the parametric range $0.039 \leq \delta/D \leq 10$ and $0.062 \leq \theta_m \leq 0.29$. Care must therefore be taken when extrapolating this expression to field conditions e.g. where Shields parameters $\theta_m = O(1)$ may be reached, see Table 1.1 below. Based on a re-investigation of the experimental data set of Sumer et al. (1992), we propose a slightly modified expression:

$$T_s^* = T_s \frac{\sqrt{g(s-1)d^3}}{D^2} = \frac{1}{400}\left(\frac{\delta}{D}\right)^{0.7}\theta_m^{-1.5} \tag{1.31b}$$

The fit of the original experimental data set to both expressions (1.31*a*) and (1.31*b*) is shown in Figure 1.10. From this figure it is seen that the new expression (1.31*b*), shown in Figure 1.10*b*, slightly improves clustering of the data compared to the original expression (1.31*a*), shown in Figure 1.10*a*, though both expressions yield similar time scale predictions within the parametric range of the data. Due to the lower magnitude exponent on the Shields parameter θ_m (i.e. power -1.5 rather than -2.2) it is felt that the modified expression (1.31b) will be less prone to wild extrapolations at field scales. Based on these considerations, the scour time scale will therefore be estimated from the modified expression (1.31*b*) in what follows.

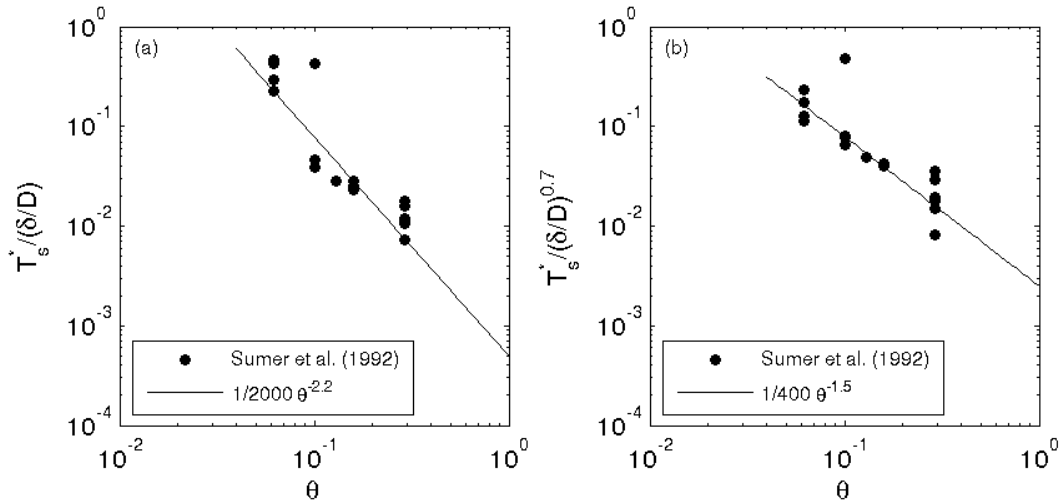

Figure 1.10. Comparison of two regression equations: (a) (1.31a) and (b) (1.31b) for predicting the time scale of scour, based on the experimental data set of Sumer et al. (1992).

The resulting values, based on the presently described parameterization, are summarized in Table 1.1, under the "full scale" column. Both dimensional, as well as dimensionless, quantities are tabulated. Importantly, it can now be ascertained that the tsunami period-to-scour time scale ratio $T/T_s = 0.54 = O(1)$ i.e. typical tsunami periods can be expected to be the same order of magnitude as expected scour time scales. This is an important recognition, and implies that the scouring process induced by tsunami events may, or may not, be of sufficient duration to reach equilibrium scour

conditions. Either scenario seems realistic, as equilibrium scour conditions can require several scour time scales to be reached.

Table 1.1. Comparison of resulting dimensional (above dashed line) and dimensionless (below dashed line) quantities at selected field and simulated model conditions, based on a diameter length scaling factor λ=50. Dimensionless quantities maintained at both scales are highlighted in bold. The equilibrium scour depth S below has been estimated from (1.24).

	Full scale	**Model scale**
D	5 m	0.1 m
d	0.3 mm	0.17 mm
T	13 min = 780 s	52.9 s
U_m	2.1 m/s	0.297 m/s
U_f	0.0745 m/s	0.0146 m/s
δ	2.36 m	0.047 m
T_s	1449 s	76.4 s
S	1.49 m	0.0297 m
s	**2.65**	**2.65**
$\boldsymbol{Fr_D}$	**0.30**	**0.30**
$\boldsymbol{\delta/D}$	**0.47**	**0.47**
KC	328	157
$Re_D=U_mD/\nu$	10^7	3×10^4
θ_m	1.1	0.078
T/T_s	0.54	0.69
$\boldsymbol{S/D}$	**0.297**	**0.297**

Based on the above discussion, we will now attempt to establish similarity between model and field scale processes. We will base our considerations on a length scaling factor λ=50 i.e. such that the monopile diameter considered at model scales will now correspond to D=5 m/λ=0.10 m. Note that this diameter is of the same order of magnitude as used in the previously discussed model validation in Section 1.4. For model scale simulations we will additionally maintain the sediment grain diameter d=0.17 mm utilized in the previously discussed model validation, corresponding to fine sand grains.

As discussed previously, due to their generally long periods, it is expected that the flow and resulting scour process around a monopile during a tsunami event will more closely resemble those under steady flow conditions, rather than those beneath wind waves. Therefore, to achieve hydrodynamic similarity we will select the flow parameters U_m and T such that we maintain similarity in terms of the diameter-based Froude number (1.27), as well as the boundary layer thickness-to-diameter ratio δ/D, based on (1.26). Equating the Froude number (1.27) ensures that the adverse pressure gradient induced by the presence of the structure itself will be similar at both model and field scales, i.e. that the ratio of the excess stagnation pressure head in front of the monopile $U_m^2/(2g)$-to-pile diameter D will be maintained. Similarly, by maintaining similarity in δ/D, we ensure that the relative size of the horseshoe vortex, which is expected to largely govern the scouring process, will be similar at both model and full scales. Maintaining similarity in terms of these two dimensionless quantities results in a model scale wave period T=52.9 s, and a velocity magnitude U_m=0.297 m/s. It can be noted that, consistent with the notion that tsunamis are much longer than wind waves, the resulting period is significantly longer than those typically used in model-scale scour experiments involving wind waves, which would typically involve periods $T=O(1\text{ s})$.

The resulting dimensional and dimensionless parameters based on the discussed "model scale" are likewise summarized in Table 1.1, in addition to the "full scale" results discussed previously. The dimensionless quantities maintained at both full and model scales are highlighted in bold. The methodology described herein is designed to yield *hydrodynamic* similarity at model and full scales. However, as can be seen from Table 1.1, it does not yield precise similarity in all other dimensionless parameters. As is well-known, the Reynolds number is obviously not maintained, though this is not expected to greatly influence the scour process. Additionally, e.g. the expected Shields parameter at model scale is an order of magnitude below that expected at full scale. Both are above critical, however, hence both conditions can be considered as effectively in the live bed scour regime. These differences are also accounted for, at least in part, in the dimensionless period-to-scour time scale ratio T/T_s, which while not identical (0.54 versus 0.69), is quite close at both full and model scales. Hence, the morphological process occurring over an individual wave period at model scale will represent a similar portion of the scour process as expected at full scale.

1.6. Simulation of tsunami-induced scour

Based on the preceding section, we will now simulate the tsunami-induced scour process around a monopile using the previously described and validated fully-coupled CFD numerical model. The idealized flow induced by our prototypical tsunami event will be introduced via the inlet (left hand) boundary (see again Figure 1.2) by prescribing the horizontal velocity u, the turbulent kinetic energy density k, and the specific dissipation rate ω, using the oscillatory wave boundary conditions proposed by Liang and Cheng (2005):

$$u = U_m \sin\left(\frac{2\pi}{T}t\right), \tag{1.32}$$

$$k = k_m\left[\sin\left(\frac{2\pi}{T}t\right)\right]^2, \quad k_m = 0.0005U_m^2, \tag{1.33}$$

$$\omega = \omega_m\left|\sin\left(\frac{2\pi}{T}t\right)\right|, \quad \omega_m = \frac{k_m}{100\nu}. \tag{1.34}$$

For the purposes of our numerical model experiment, the "model scale" parameters presented previously in Table 1.1 (i.e. U_m=0.297 m/s and T=52.9 s) will be utilized to drive the simulation. Three full tsunami periods will be simulated in succession. The motivation for considering multiple periods is three-fold: First, a real-life tsunami may well consist of a leading wave, in addition to several trailing waves; Second, consideration of the successive periods will shed light on tsunami-induced scour in the presence of pre-existing scour holes; Third, this will increase the effective total scour time, and hence can be considered relevant e.g. for other tsunami events having longer period than that specifically being considered herein. As an indication of computational time for the present simulation, each successive model-scale period requires approximately 10 days of CPU time, when simulated in parallel on eight modern processors i.e. the full simulation requires approximately one month to complete.

The simulated time series of the scour depth, taken at both the front and back face of the monopile, are first presented in Figure 1.11*b*. As a useful reference for the corresponding flow, the free stream velocity time series is also presented in Figure 1.11*a*. It is seen from Figure 1.11*b* that the first half-cycle (flow going rightward) expectedly produces significant scour at the front (left) side, which is then followed by a similar scouring process on the back (right) side during the second half-cycle

(flow going leftward). These scouring processes can be mainly attributed to separate horseshoe vortices forming on opposite sides during the two successive half cycles. Due to the relatively long times involved, the processes occurring during the two half cycles seem to be largely independent of one another. It should be noted that, in the present scenario, the first half-cycle may be taken as either representing a leading elevation or leading depression tsunami wave, depending on the orientation adopted.

Beyond the first period, it is seen that the scour deepens at both front and back sides during the successive wave periods in a loosely stepwise fashion i.e. the observed scour process can be characterized as largely cumulative. Some minor stages of backfilling are also observed on the front side of the monopile. These consistently occur around the time of, or just after, the flow reversal, and are hence generally consistent with trends seen e.g. from the previously considered steady current case (Figure 1.8), which illustrates a tendency for relatively smaller lee-side scour depths. Note that this backfilling only occurs here on the front face, where the relatively large scour hole just induced by the previous (rightward-directed) flow subsequently becomes the lee side following the flow reversal.

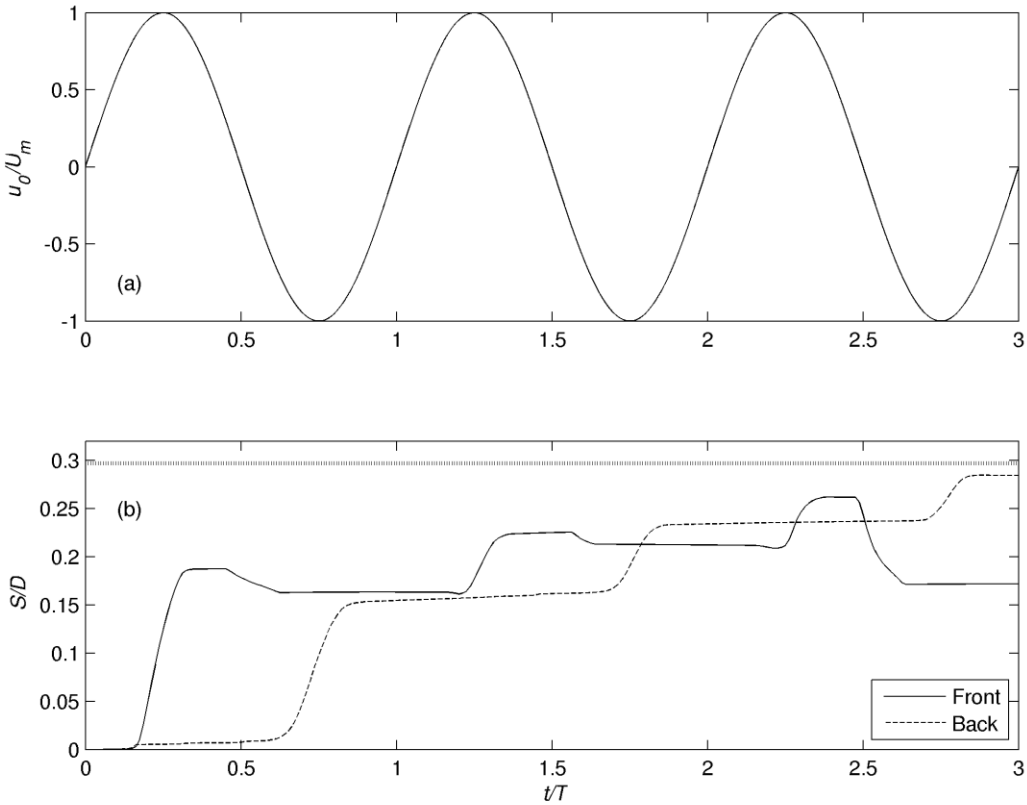

Figure 1.11. Computed time series of (a) free stream velocity and (b) scour depth at the front and back face of the monopile. The horizontal dashed line in (b) represents the equilibrium scour depth estimated from (1.24).

As a reference value, the equilibrium scour depth predicted by (1.24), after invoking (1.26), yields S/D=0.297. This value is also depicted in Figure 1.11*b* as the horizontal dashed line. As seen, after several periods of accumulation the resulting scour on both sides of the monopile seems to be

gradually approaching this equilibrium value. Note that the relatively moderate equilibrium scour (at least in dimensionless terms i.e. $S/D<0.3$) predicted in the present case, is due to the finite boundary layer thickness-to-diameter ratio $\delta/D=0.47$, which limits the relative size of the formed horseshoe vortices. Invoking the full scale monopile diameter $D=5$ m, however, this still correspond to considerable scour i.e. up to approximately $S=1.5$ m for the full scale conditions considered. Based on the cumulative nature of the present results, it is reasonable to expect that the scour around a monopile will continue to build over the duration of a given tsunami event, ceasing when equilibrium scour depths are reached, which will occur only if the event is sufficiently long. Additionally, the effects on the scour associated with finite boundary layer thickness seem to be reasonably accounted for by the steady current expression (1.24), after invoking the tsunami wave boundary layer thickness from (1.26).

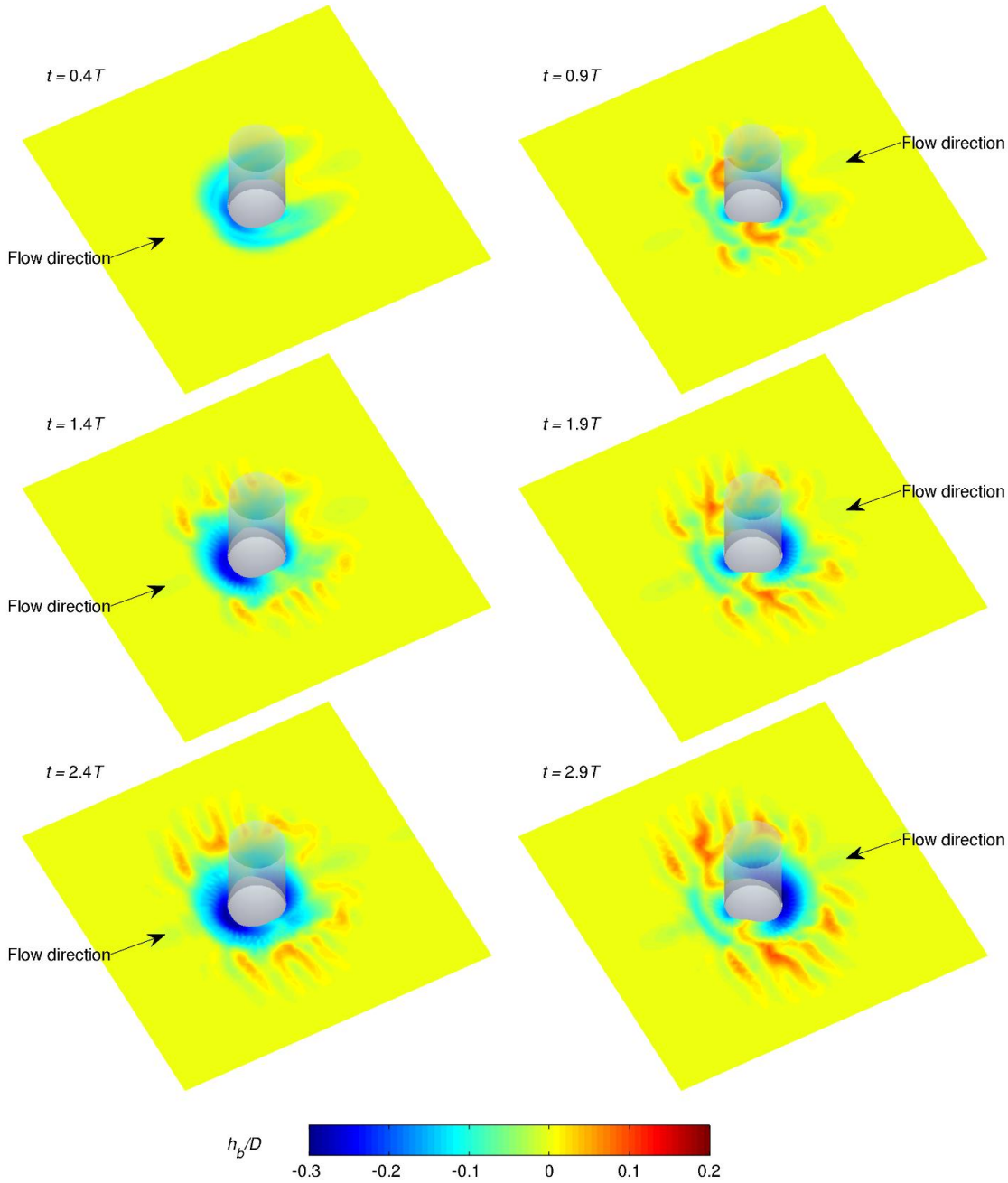

Figure 1.12. Snapshots of the computed tsunami-induced scour at selected times. The colorbar refers to the dimensionless sea bed elevation h_b/D.

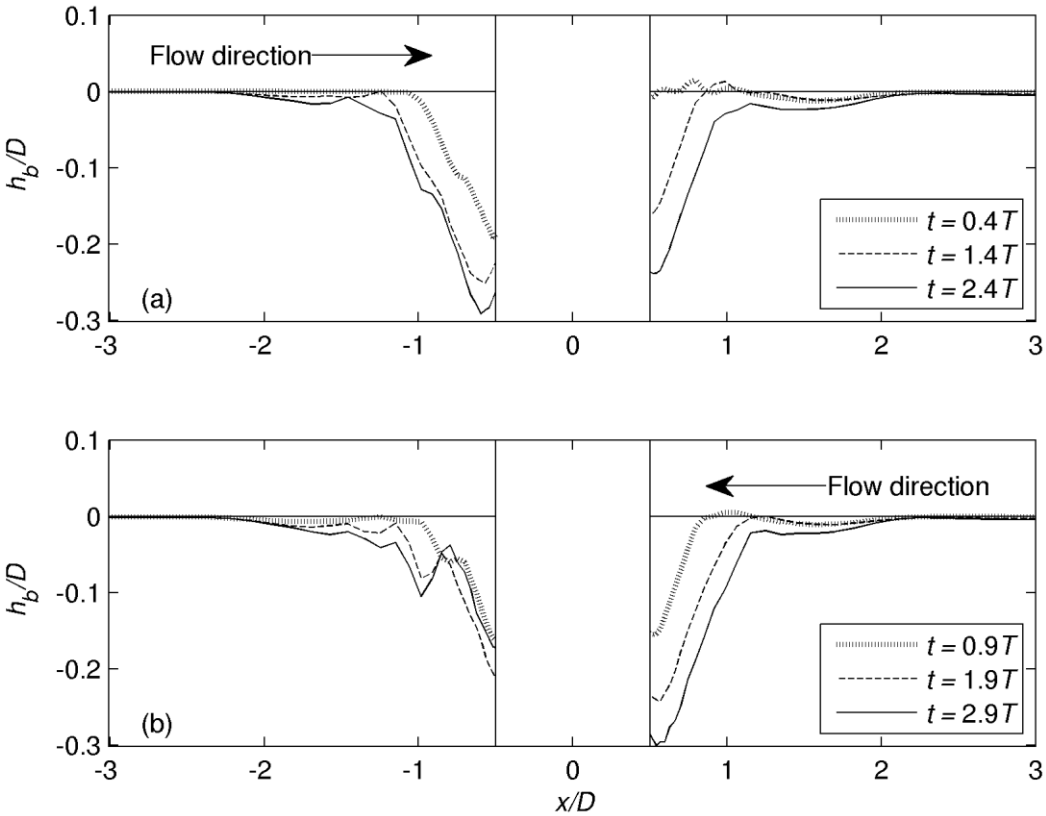

Figure 1.13. Computed bed profiles along the centerline *y*=0 at selected times when the flow is (a) rightward and (b) leftward; The times selected correspond to shown in Figure 1.12. Note that the vertical scale is grossly exaggerated.

Snapshots of the computed scour holes at selected times when the flow is leftward (*t*=0.4*T*, 1.4*T*, and 2.4*T*) as well as rightward (*t*=0.9*T,* 1.9*T*, and 2.9*T*) are additionally depicted in Figure 1.12. These figures likewise illustrate the generally stepwise buildup of scour on the two opposing sides of the monopile during each successive half-cycle of the simulated tsunami (see again Figure 1.11*b*). In addition to the scour occurring on the front and back faces of the monopile, small scale "ripple-like" features are also seen develop, first to the transverse sides of the monopile, and then alternatively to the front and back of the monopile as time progresses. Such features tend to initially form during the flow reversal, due to settling of suspended sediments. They are generally less prevalent than were observed e.g. in the steady current case (e.g. Figure 1.6), presumably due to limited growth time, in combination with the lower far-field Shields parameters reached in the present case (presently 0.078 versus 0.13 for Figure 1.6). It should be noted that at full field scales, sheet flow conditions may in fact be reached, corresponding to θ_m=*O*(1) (see Table 1.1). Hence, the small scale ripple features developing in the present (model scale) result may in fact be related to scale effects. In any event, they do not seem to dramatically affect the overall scour process.

The computed scour profiles along the model centerline (*y*=0), taken at the same instances as depicted in Figure 1.12, are similarly depicted in Figure 1.13. To ease comparison, these have been divided into times when the flow is leftward (Figure 1.13*a*, corresponding to the left-hand subplots of Figure 1.12) and rightward (Figure 1.13*b*, corresponding to the right-hand subplots on Figure 1.12). Inspection of the scour profiles, as a whole, demonstrates that reasonable symmetry is maintained throughout the scour process, consistent with the symmetric nature of the idealized

(sinusoidal) flow description utilized in the present Chapter. The asymmetry observed at any particular time is primarily due to the directionality of the flow (i.e. rightward or leftward directed) just experienced. Based on the present results, in real (less idealized) tsunami events the asymmetry of the scour profile can be expected to depend strongly on the asymmetric nature of individual tsunami waves, which can of course vary widely from event to event. Considering the present results at half- and full-period intervals should provide a reasonable first indication regarding expected scour asymmetry, however.

1.7. Practical model for predicting tsunami-induced scour

As it is not always feasible in practice to perform advanced fully-coupled CFD simulations of tsunami-induced scour processes (even at model scales), especially for a large number of scenarios, it is of major importance that simpler methods be developed for predicting the tsunami-induced scour around monopile foundations in engineering practice. Such a simple practical method will be developed in the present section, which will utilize existing physical scour process knowledge, while also incorporating additional insight gained from the numerical simulation of the scour process presented in Section 1.6.

To begin making a practical assessment on the expected tsunami-induced scour around a monopile foundation, it is convenient to first estimate the maximum expected equilibrium scour that would be expected to occur at infinite time i.e. if a given tsunami event was repeated indefinitely. Taking into account the effect of a (potentially finite) boundary layer thickness-to-pile diameter ratio δ/D, and taking inspiration from (1.24), this equilibrium scour S_δ can be reasonably estimated according to (Sumer and Fredsøe, 2002, Eq. 3.11):

$$\frac{S_\delta}{D} = \frac{S_0}{D}\left(1 - \exp\left\{-0.55\frac{\delta}{D}\right\}\right), \tag{1.35}$$

where the tsunami wave boundary layer thickness δ can be estimated directly from (1.26), and where the maximum potential current-induced scour (for large boundary layer thickness) may be taken as

$$\frac{S_0}{D} = 1.3 \pm \sigma_{S/D}\,. \tag{1.36}$$

Here $\sigma_{S/D}$=0.7 is the standard deviation of expected scour, as presented by Sumer et al. (1992), which can be accounted for in practice to adjust for a desired level of conservativeness. In what follows, we aim to predict the mean expected scour, hence this standard deviation will be neglected i.e. we simply utilize S_0/D=1.3 in (1.35).

Now, as emphasized previously, typical tsunami periods can be expected to be the same order of magnitude as expected scour times scales. This, again, implies that true equilibrium scour depths may, or may not, be reached, depending on the duration of a given tsunami event, since reaching equilibrium can require several scour time scales. It is therefore important to take the expected time development of the scour process into account when making tsunami-induced scour predictions. Utilizing a scour time scale T_s estimated from (1.31*b*), this temporal variation can then be described according to the following expression

$$\frac{S}{D} = \frac{S_\delta}{D}\left(1 - \exp\left(-\frac{t_s}{T_s}\right)\right), \quad t_s = n\psi T, \tag{1.37}$$

which is commonly used to characterize typical time development of scour processes. In the equation above t_s represents the effective scour time, and n represents the integer number of successive waves characterizing a given tsunami i.e. n=1 can be utilized to predict the maximum scour occurring during the leading tsunami wave, with n=2,3,… utilized for predicting the accumulated scour induced by any successive waves. The additional factor $\psi \leq 1$ can be taken to represent the effective scouring fraction of a period, though in what follows we utilize $\psi = 1$, for simplicity. Note that for large t_s, (1.37) will simply lead to equilibrium scour i.e. $S = S_\delta$.

To test the validity of the simple practical model described above, the predicted scour from the practical approach leading to (1.37) will be compared directly with the numerical scour results presented in Section 1.6. To directly test the scour time development of the simple practical model, accumulated scour results from each of the three successive wave periods in the simulation (see Figure 1.11*b*) will be considered separately, with the results corresponding to the maximum scour occurring during a given period of interest. Results at both the front and back face of the monopile will be considered separately, for completeness. A plot summarizing the computed versus predicted (utilizing the present simple practical approach) maximum scour (circles) is depicted in Figure 1.14.

It is emphasized that the approach proposed above is conveniently founded upon existing experimentally-based expressions for use in steady current scour, but invoking the boundary layer thickness and Shields parameter expected from tsunami wave events i.e. it effectively combines both current-like and wave-like properties of tsunamis. As such, at the infinite period limit, the practical model proposed is fully consistent with existing methodology for predicting equilibrium scour under steady current conditions. Therefore, for completeness, the computed and predicted equilibrium value for the simulated current-induced scour (Section 1.4), previously considered as model validation, is also shown (square) in Figure 1.14.

As can be seen, the simple predictive model proposed above does a consistently good job of predicting the scour observed within the numerical simulations, with all results near the line of perfect agreement (full line) in Figure 1.14. This conclusion holds for the full range of flows considered: For the transient tsunami cases, though the simple model cannot predict all details, such as the momentary lee-side backfilling episodes observed on the front face, it adequately predicts the accumulative maximum scour occurring over the three successive tsunami periods. As discussed previously, relatively moderate S/D values are found for the tsunami scenario considered, owing to effects associated with the finite boundary layer thickness, which seem to be properly accounted for. Such effects become negligible at the steady current limit, leading to the larger S/D, which is also adequately captured by the proposed simple approach.

It is finally important to emphasize that the steady current limit can be considered quite physically relevant for scenarios involving tsunami-induced scour in many circumstances, at least as a first approximation. In particular, this limit would seem particularly relevant for tsunamis having very long duration (i.e. large T/T_s), for scour occurring at shallower water depths (where the boundary layer thickness δ can be taken as equivalent to the water depth h), or for tsunami-induced scour around smaller monopile diameters (i.e. where the boundary layer thickness-to-pile diameter ratio becomes large i.e. δ/D>4) e.g. those more typical of bridge piers. Hence, the full range of flows considered in this Chapter can indeed be considered as tsunami-relevant in practice.

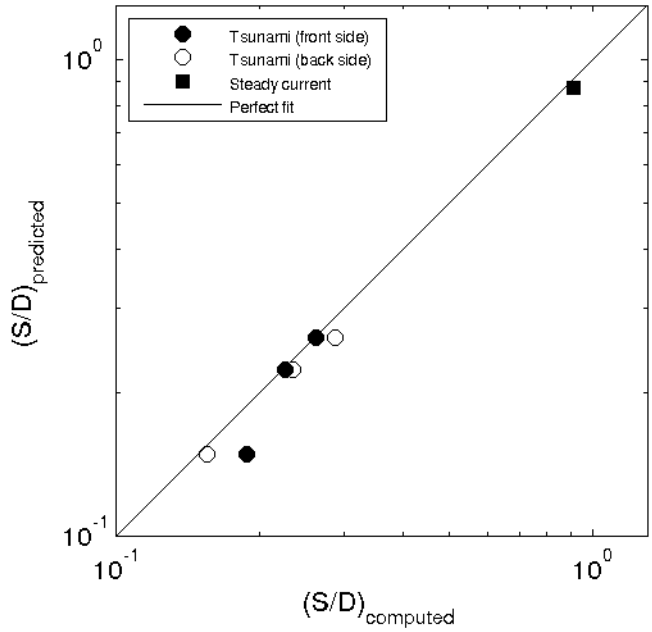

Figure 1.14. Comparison of computed scour depths with those predicted by the practical model. The tsunami cases depict the maximum scour depth (at both front and back sides) that occur during 1, 2, and 3 successive wave cycles. Also shown is the steady current result from Section 1.4.

1.8. Conclusions

This Chapter presents a numerical assessment for tsunami-induced scour around a monopile structure, as commonly utilized in practice as offshore wind turbine foundations. The basis of the numerical model is the advanced fully-coupled hydrodynamic and morphological CFD model presented in Jacobsen et al. (2014), and utilized specifically for simulating scour processes by Baykal et al. (2015) and Fuhrman et al. (2014). The model hydrodynamics are based on Reynolds-averaged Navier-Stokes (RANS) equations, coupled with two-equation k-ω turbulence closure. These are then coupled with both bed and suspended sediment transport descriptions, which drive resultant morphology of the sea bed. Some recent results of Baykal et al. (2015) have been presented here, as relevant model validation, for simulated flow and scour processes around a monopile under steady current conditions.

Due to computational expense, it is only feasible at present to simulate scour processes at model (laboratory) spatial and temporal scales. Therefore, prior to making any simulations, a methodology has been developed for establishing similarity (based on dimensionless numbers) between full tsunami and model scales, in precisely the same fashion as in hydraulic scale model experiments in which similarity is established between full scale real life and the hydraulic scale model. This methodology is based on a diameter-based Froude number, coupled with the dimensionless ratio of the expected boundary layer thickness-to-monopile δ/D diameter. The Froude similitude ensures similarity in the adverse pressure gradients induced by the presence of the structure itself, whereas the δ/D similarity ensures equivalent relative size of the horseshoe vortex in front of the monopile. Reasonable morphologic similarity of the scour process is also maintained, by ensuring that the dimensionless tsunami period-to-scour time scale ratios are similar. It is demonstrated that typical tsunami periods can be expected to be the same order of magnitude as expected scour time scales in real life. This implies that equilibrium scour conditions may, or may not, be reached, depending on the total duration of a given tsunami event.

Taking a well-known tsunami measurement from the 2004 Indian Ocean tsunami as a typical event at full scale (in terms of its surface amplitude and approximate period), input parameters are found based on the similarity principles described above. These are then utilized within simulations of the tsunami-induced scour process around a monopile foundation. The results generally demonstrate that, consistent with physical expectations due to their long periods, the tsunami-induced scour process reasonably resembles that under steady current conditions. Unlike steady current scour, however, the tsunami-induced scour process, under the conditions considered, can be limited by finite wave boundary layer thickness, rather than the flow depth. Hence, it is important to take into account both the current-like (due to their long periods), as well as their wave-like (unsteady) properties, to fully understand and assess the tsunami-induced scour process.

Based on existing scour knowledge, combined with the insight gained from the advanced CFD simulations, a simple methodology has been developed for predicting tsunami-induced scour around monopiles in practice. The method takes into account the time variation of the scour process, and can hence be applied to predict the cumulative tsunami-induced scour under successive periods i.e. it is not limited to simply a leading wave description. The practical method makes modified use of existing experimentally-based expressions for predicting steady current scour and time scales, and hence is fully-consistent with these at this (infinite period) limit. The practical method is demonstrated to accurately predict all of the simulated scour depths considered in the present Chapter i.e. ranging from the simulated transient tsunami events to that induced by steady current flows.

1.9. References

Aydin, D.C., Dogan, G.G., Tarakcioglu, G.Ö., Yalciner, A.C. and Dogulu, N. (2014) *Lessons From Recent Tsunamis Impacts on Coastal and Marine Structures and Coastal Utilities, and Performance of Mitigation Strategies*. ASTARTE, Deliverable 5.3.

Baker, C.J. (1979) The laminar horseshoe vortex. *J. Fluid Mech.* **95**, 344—367.

Baykal, C., Sumer, B.M., Fuhrman, D.R., Jacobsen, N.G. and Fredsøe, J. (2015) Numerical investigation of flow and scour around a vertical circular cylinder. *Phil. Trans. Roy. Soc. A* **373**, 20140104.

Bricker, J.D., Francis, M. and Nakayama, A. (2012) Scour depths near coastal structures due to the 2011 Tohoku tsunami. *J. Hydraul. Res.* **50**, 637—641.

Cebeci, T. and Chang, K.C. (1978) Calculation of incompressible rough-wall boundary-layer flows. *AIAA J.* **16**, 730—735.

Chan, I.-C. and Liu, P.L.-F. (2012) On the runup of long waves on a plane beach. *J. Geophys. Res.* **117**, C08006.

Chen, J., Huang, Z., Jiang, C., Deng, B. and Long, Y. (2013) Tsunami-induced scour at coastal roadways: a laboratory study. *Nat. Hazards* **69**, 655—674.

Engelund, F. and Fredsøe, J. (1976) A sediment transport model for straight alluvial channels. *Nord. Hydrol.* **7**, 293—305.

Engelund, F. and Fredsøe, J. (1982) Hydraulic theory of alluvial rivers. *Adv. Hydrosci.* **13**, 187—215.

Fuhrman, D.R., Schløer, S. and Sterner, J. (2013) RANS-based simulation of turbulent wave boundary layer and sheet-flow sediment transport processes. *Coast. Eng.* **73**, 151—166.

Fuhrman, D.R., Baykal, C., Sumer, B.M., Jacobsen, N.G. and Fredsøe, J. (2014) Numerical simulation of wave-induced scour and backfilling processes beneath submarine pipelines. *Coast. Eng.* **94**, 10—22.

Hjorth, P. (1975) *Studies on the nature of local scour*. Lund Institute of Technology, University of Lund, Bulleting Series A, no. 46, viii edn. Lund, Sweden: Department of Water Resources Engineering.

Jacobsen, N.G., Fredsøe, J. and Jensen, J.H. (2014) Formation and development of a breaker bar under regular waves. Part 1. Model description and hydrodynamics. *Coast. Eng.* **88**, 182—193.

Justesen, P., Fredsøe, J. and Deigaard, R. (1986) The bottleneck problem for turbulence in relation to suspended sediment in the surf zone. In: *Proc. 20th Int. Conf. on Coast. Eng.*, Taipei, Taiwan, pp. 1225—1239.

Liang, D. and Cheng, L. (2005) Numerical model for wave-induced scour below a submarine pipeline. *J. Waterw. Port Coast. Ocean Eng.-ASCE* **131**, 193—202.

Madsen, P.A. and Fuhrman, D.R. (2008) Run-up of tsunamis and long waves in terms of surf-similarity. *Coast. Eng.* **55**, 209—223.

Madsen, P.A., Fuhrman, D.R. and Schaffer, H.A. (2008) On the solitary wave paradigm for tsunamis. *J. Geophys. Res.* **113**, C12012.

Nakamura, T. and Mizutani, N. (2014) Sediment transport calculation considering laminar and turbulent resistance forces caused by infiltration/exfiltration and its application to tsunami-induced local scouring. *J. Offshore Mech. Arctic Eng.-ASME* **136**, 011105.

Pan, C. and Huang, W. (2012) Numerical modeling of tsunami wave run-up and effects on sediment scour around a cylindrical pier. *J. Eng. Mech.* **138**, 1224—1235.

Roulund A., Sumer, B.M., Fredsøe, J. and Michelsen, J. (2005) Numerical and experimental investigation of flow and scour around a circular pile. *J. Fluid Mech.* **534**, 351—401.

Sumer, B.M., Fredsøe, J. and Christiansen, N. (1992) Scour around a vertical pile in waves. *J. Waterw. Port. Coast. Ocean Eng.-ASCE* **117**, 15—31.

Sumer, B.M. and Fredsøe, J. (2002) *The Mechanics of Scour in the Marine Environment*. World Scientific, Singapore.

Tonkin, S., Yeh, H., Kato, F. and Sato, S. (2003) Tsunami scour around a cylinder. *J. Fluid Mech.* **496**, 165—192.

Van Dreist, E.R. (1956) On turbulent flow near a wall. *J. Aeronaut. Sci.* **23**, 1007—1011, 1036.

Wilcox, D.C. (2006) *Turbulence Modelling for CFD*. 3rd ed., DCW Industries, La Canada, CA.

CHAPTER 2. TSUNAMI IMPACTS ON AQUACULTURE

2.1 Introduction

In this chapter, the aim is to provide an overview on the tsunami impacts on aquaculture rather than presenting a comprehensive review on the status and trends in aquaculture development. [For such a comprehensive review the reader is referred to the FAO (Food and Agriculture organization of the United Nations) report titled "The State of the World Fisheries and Aquaculture" released in May 2014.] For this purpose, we first briefly provide and introductory summary on aquaculture. This is followed by the section "Vulnerability of Fisheries and Aquaculture Systems" where the main focus is the vulnerability to tsunamis. Next, tsunami Impacts on aquaculture are exemplified based on the major tsunami events that occurred since 2000s. Later, specific case studies highlighting different aspects in aquaculture design are illustrated in the section "Engineering Design of Aquaculture Systems".

2.2 Aquaculture

Aquaculture (aquafarming) is "the farming of aquatic organisms including fish, molluscs, crustaceans and aquatic plants" (FAO, 2014a). According to the NOAA Aquaculture Office (2014), aquaculture refers to "the breeding, rearing, and harvesting of plants and animals in all types of water environments". Aquaculture differs from commercial fishing in that in aquaculture freshwater and saltwater populations are cultivated under controlled conditions whereas in commercial fishing wild fish is directly harvested.

Among the particular kinds of aquaculture are the following: fish farming, shrimp farming, oyster farming, mariculture, algaculture (such as seaweed farming), and the cultivation of ornamental fish (Wikipedia). The most economically important form of aquaculture is fish farming, an industry that accounts for an ever increasing share of world fisheries production (Columbia Encylopedia). It is important to distinguish between mariculture and freshwater aquaculture:

- ***Mariculture*** is a specialized branch of aquaculture practiced in marine environments and in underwater habitats. It involves the cultivation of marine organisms for food and other products in the open ocean or an enclosed section of the ocean (i.e. in cages, on the seafloor, or suspended in the water column) or in on-land, manmade systems such as ponds, tanks or raceways which are filled with seawater. In particular, the farming of marine fish is an example of mariculture, and so also is the farming of marine crustaceans (such as shrimps), molluscs (such as oysters) and seaweed.
- ***Freshwater aquaculture*** produces species that are native to rivers, lakes, and streams. Freshwater aquaculture takes place primarily in ponds and in on-land, manmade systems such as recirculating aquaculture systems.

Some examples to marine aquaculture can be seen in Figure 2.1.

(a) (b)

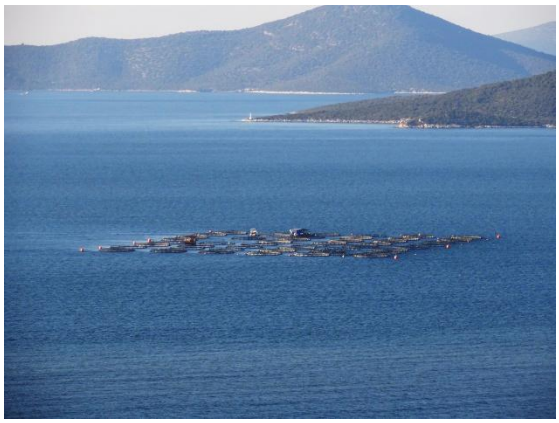

©

Figure 2.1. Marine aquaculture examples: (a) An offshore aquaculture plant in Gulluk Bay, Turkey, (b) Salmon pens off Vestmanna – Faroe Islands, Denmark, (c) An offshore aquaculture plant in Gulf of Mexico. [Photo Credit: (a) Ahmet Cevdet Yalciner, Sena Acar – METU, (b) Erik Christensen – Wikipedia, (c) Snapperfarm – NOAA Fisheries Southeast Regional Office].

Some facts around the world:

- Fisheries and aquaculture support the livelihoods of some 60 million people in Asia and Africa (FAO, 2014b).
- While aquaculture production was nearly 80 million tonnes in 2010 (see Figure 2.1a), in 2012, aquaculture production globally reached a record high of more than 90 million tons (FAO, 2014a).
- Aquaculture is an especially important economic activity in China. Figure 2.2a shows the global aquaculture production by country (million tonnes) between the years 1950 - 2010. It can be clearly noticed that China stands out with 45 million tonnes of aquaculture production. In 2010, China was responsible for the 61% of the total aquaculture production. In 2012, China is the top-ranking fishing country in terms of quantity followed by Indonesia, the United States of America, India and Peru (FAO, 2014a).

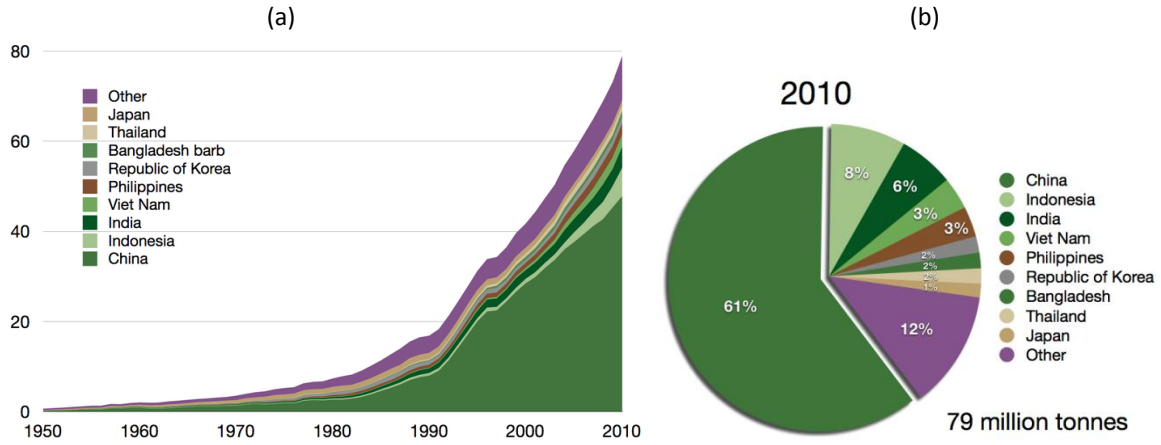

Figure 2.2. (a) Global aquaculture production by country in million tonnes, 1950–2010, as reported by the FAO, (b) Global aquaculture production by country for 2010 (Based on data sourced from the FishStat database).

- World marine capture production Global fishery production in marine waters was 82.6 million tonnes in 2011 and 79.7 million tonnes in 2012. Most of the Asian countries have shown considerable increases in marine catches in the last 10 years, with the exception of Japan and Thailand, which have registered decreases, and the Philippines and the Republic of Korea, whose catches have grown slightly (FAO, 2014b).
- Production distribution Worldwide, 15 countries produced 92.7 percent of all farmed food fish in 2012. Among them, Chile and Egypt became million-tonne producers in 2012 (FAO, 2014b).

2.3 Vulnerability of fisheries and aquaculture systems

Noting the growing recognition of the role that fisheries and aquaculture play in providing the world's growing population with both food and livelihoods, it becomes essential to identify and assess vulnerability of fisheries and aquaculture systems, and consider design approaches resistant to such vulnerabilities.

Table 2.1 shows different types of vulnerability that fisheries and aquaculture systems reported in FAO (2014b). While climate-change related vulnerabilities pose the greatest concern for majority of the case studies, tsunamis are considered as vulnerability only for the Caribbean region.

The increasing number and intensity of natural disasters severely influences people who depend on fisheries and aquaculture for their livelihoods. Considering the location and exposure characteristics of fishing and fish farming operations the vulnerability of aquaculture to water-related hazards is greatly amplified (FAO, 2014c). In an attempt to assist countries and organizations responding to a disaster emergency, FAO recently published a guidance document devoted to fisheries and aquaculture sector. The document, titled "Fisheries and aquaculture emergency response guidance", draws on best practice and lessons learned during response to disasters (including water-related hazards) that have affected fisheries and aquaculture sector.

Table 2.1. Vulnerability of fisheries and aquaculture systems (FAO, 2014b).

	Vulnerability										
	Overfishing	Drought	Variation in rainfall	Sea-level rise	Variation in sea surface temperature	Variation in currents	Acidification	Extreme weather events	Flooding	Changes in land use, damming	Volcanic eruptions, landslides, tsunamis
Lake Chad fisheries and farming		■	■								
Caribbean fisheries			■	■	■		■	■			■
Caribbean aquaculture							■	■	■		■
Mekong fisheries				■						■	
Mekong aquaculture									■	■	
Mekong rice				■					■	■	
Benguela fisheries	■					■					
Pacific fisheries					■		■				
Pacific aquaculture											
Pacific coastal habitats					■		■				
Latin America fisheries	■				■			■			
Latin America aquaculture							■	■		■	

FAO has published tsunami specific documents and reports focusing on the policy and management aspects of fisheries and aquaculture as well. The two prominent examples to such publications are "Regional strategic framework for rehabilitation of fisheries and aquaculture in tsunami affected countries in Asia" (FAO, 2005) and "One year later – The rehabilitation of fisheries and aquaculture in coastal communities of tsunami affected countries in Asia" (FAO, 2006). These two documents provide valuable insights based on the experience gained with the disaster caused by the tsunami waves following the earthquake on 26 December 2004, in Sumatra. This chapter is not intended to provide a detailed overview of the regional strategic framework presented in FAO (2005), and the recommendations for action in tsunami rehabilitation listed in FAO (2006). However, we kindly invite the readers who have particular interest in the topics to refer to these documents when the need arises.

2.4 Tsunami impacts on aquaculture

Tsunamis pose a great risk to aquaculture operations. These risks can be listed as follows (FAO, 2014c): (i) coastal aquaculture plant - extensive drag force by tsunami current and uplift force by water level rise, (ii) offshore aquaculture plant extensive drag force by tsunami current and uplift force by water level rise, (iii) collapse and damage on supporting structures and other structural components (ropes, chains, piles and other components) of aquaculture plants, and (iv) silting and deposition of sediment and debris (due to tsunami action) in fish living nets and ponds.

Next, more specific examples of tsunami impacts on aquaculture are given.

The earthquake and tsunami of 26 December 2004

- In Sri Lanka and Indonesia fisheries and aquaculture were the sectors most severely hit by the disaster – which destroyed or damaged many boats, fishing gear, ponds and support installations (FAO, 2007). The FAO (2007) report is the outcome of the project "A rapid assessment of the status of the fisheries in tsunami affected areas of Indonesia and Sri Lanka (OSRO/RAS/504/LAO)" – which is aimed to provide technical advice to enhance knowledge of the impact of the tsunami on a limited number of affected inshore fisheries habitats and marine resources.

(a)

(b)

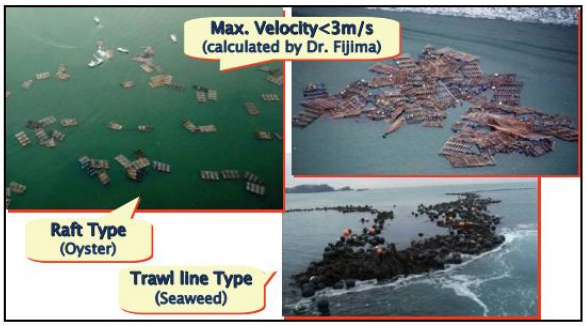

(c)

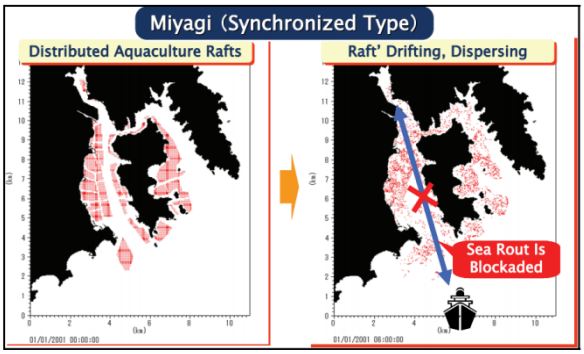

(d)

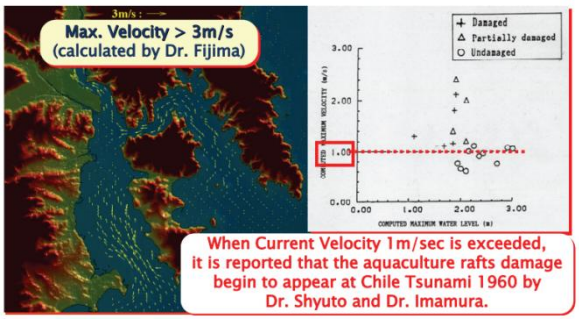

Figure 2.3. The 2010 Chile earthquake and tsunami: (a) fishing vessels hurled inland, (b) drift simulation of the aquaculture rafts, (c) damage of aquaculture rafts, and (d). [Photo Credit: (a) Mercator Media, 2015, (b)-(c)-(d) Otsuka et al., 2009.]

Tsunami by Chile earthquake 2010

- The 2010 Chile earthquake (on 27 February 2010) and tsunami destroyed more than 70% of Chile's central-south coastal fishing fleet (World Fishing and Aquaculture, 2010). In Chile, the fishing vessels were thrown inland (Figure 2.3a).
- Chilean tsunami also damaged the city of Kesennuma in Japan. As can be seen in Figure 2.3b, many aquaculture rafts were heavily damaged mainly due to driftage (Otsuka et al., 2009). An example of drift simulation for the aquaculture rafts can be seen in Figure 2.3c.

- Tsunami current simulation for the Kesennuma Bay by Otsuka et al. (2009) is shown in Figure 2.3d. The maximum current velocity, based on the calculations of Dr. Fujima, was over 3 m/s. It should be noted that in 1960 Chile Tsunami the threshold current velocity was 1 m/s for which the aquaculture rafts damage begins to appear.

The Great East Japan Earthquake and Tsunami in 2011

- The earthquake and tsunami damaged some 25,000 fishing vessels, at a cost of ¥170 billion. Ninety percent of the vessels in Iwate, Miyagi, and Fukushima prefectures were damaged, which had an enormous effect on the fishing industry since these vessels were used for aquaculture as well as fishing. Damage to aquaculture amounted to ¥131 billion: 57 billion for production and 74 billion for facilities (World Bank, 2012). The damage on Japan fisheries sector is summarized in Table 2.2.

Table 2.2. Damage on Japan fisheries sector caused by the Great East Japan Earthquake and Tsunami (World Bank, 2012).

	Direct damage	*Monetary damage (¥100 million)*
Fish vessels	25,014	1,701
Fishery harbour facilities	319 harbors	8,230
Aquaculture facilities	-	738
Aquaculture products	-	575
Common use facilities	1,725 facilities	1,249

- The damage was substantially high for the Oyster farms (Figure 2.4 and 2.5) in Iwate, Miyagi, and Fukushima prefectures which accounted for about 30 percent of the nation's total, and “wakame (brown seaweed)” about 80 percent before the tsunami. Unfortunately, many of the oyster beds and other aquaculture facilities along Japan's Pacific coast suffered heavy damage from the GEJE tsunami.

Figure 2.4. An example of a commercial oyster bed in Japan – many of the oyster beds and other aquaculture facilities along Japan's Pacific coast suffered heavy damage from the GEJE tsunami. [Photo Credit: http://what-when-how.com/water-science/aquaculture-water-science/]

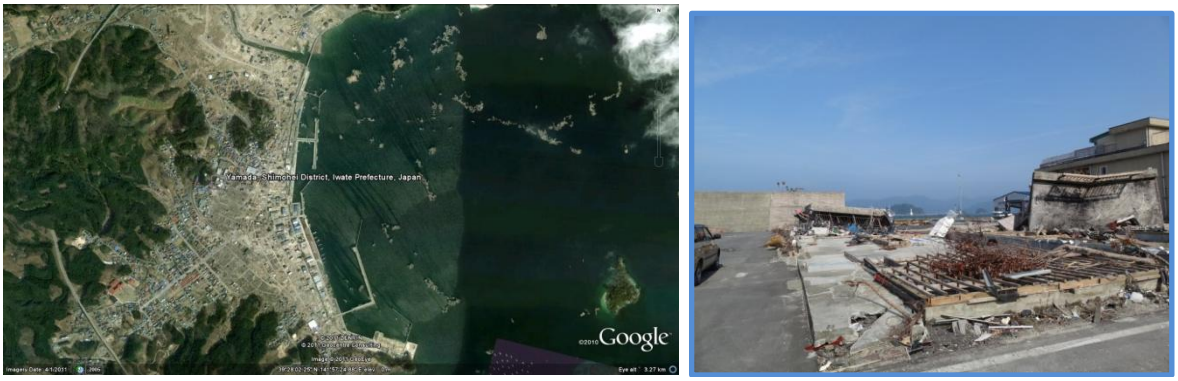

Figure 2.5. Damage on Oyster farms at Yamada Bay, Japan by 2011 GEJE Tsunami (Yalciner et al, 2011).

(a)

(b)

(c)

Figure 2.6. (a) Wreckage of shellfish culture gear and boats in Miyagi, (b) Miyako Station, Fisheries Research Agency - before the tsunami, (c) after the tsunami. [Photo Credit: (a) Walsh and Hanafusa (2013), (b) Fisheries Research Agency of Japan, (c) ©2013 DigitalGlobe, Cnes/Spot Image, Map data ©2013 Google, ZENRIN]

- Figure 2.6 shows the extent of damage in Miyagi.
- Following the destruction of fishing vessels and infrastructure, Japan's total marine capture production was forecast to fall by about one-third. However, the actual decrease in comparison to 2010 was about 7 percent, with a further decrease of 3.5 percent in 2012 (FAO, 2014b).
- Thailand, after its record-high aquaculture production of 1.4 million tonnes in 2009, saw its production fall to 1.3 million tonnes in 2010 and 1.2 million tonnes in 2011 and 2012, mainly

owing to widespread flood damage in 2011 (and the dive in shrimp yield as a consequence of early mortality syndrome). Cut to just over half a million tonnes by the 2011 tsunami, Japan's aquaculture production recovered slightly to more than 0.6 million tonnes in 2012 (FAO, 2014b).

2.5 Engineering design of aquaculture systems and tsunamis

While an important aspect of successful aquaculture includes consideration of, for example, water source and water quality studies, pond and tank containment systems, water filtration and aeration, an equally important second aspect is engineering design. Engineering design plays an important role in achieving successful aquaculture. The safety and stability of aquaculture systems need proper design against extreme conditions. Storms and storm waves are main extreme conditions causing damage on aquaculture plants. Tsunamis are rare events but they are seriously effective on any coastal plants. There are numerous studies describing design procedure of different types of aquaculture plants against storm conditions but not specifically against tsunamis. However those can be useful to develop design procedure of aquaculture plants against tsunamis.

In this section, some of those case studies concerning engineering design of aquaculture systems are summarized.

Fullerton et al. (2004) have worked on the automated feed-buoy for submerged cages which has two-hundred-fifty kilogram feed capacity. In order to permit for the tidal range and large storm waves the buoy taut-anchored above the cage. On the other hand, feeding mechanism needs an electric power pump to push down the feed to the cage. To obtain necessary electric power, wind generator and solar panels can be used. Also, controlling of the system is provided by spread spectrum radio and internet. Furthermore, seakeeping behaviour of the buoy must be characterized. To achieve this, writers measure heave and pitch responses to single frequency waves through free release tests.

Suhey et al. (2005) have investigated numerical modelling and design of inflatable structures for open-ocean-aquaculture cages by using non-linear finite element analysis of membrane structures. The finite element model is confirmed by comparing the maximum deflection and stress. Mainly, when the tension-only membrane is removed by adding an artificial shell with small stiffness, there is numerical instability. To test the stiffness and unity of the system, a full scale cage model is produced using membrane, shell and string elements. According to the test results, inflated structures have enough stiffness to be used a structural support.

Stevens et al. (2008) have widely examined the physics of open-water shellfish aquaculture, mainly effect of the flow on the farm. According to the writers, from the perspective of structural survival and wave reduction, interaction between farms and hydrodynamics is important where energy is transferred from the flow to the farm structure. One of the hydrodynamic forces is currents which considered as a steady drag force and expressed with quadratic drag relationship (Equation 1). In this equation, ρ is fluid density, A is the area, C_d is steady drag coefficient and U is mean velocity. To estimate total drag coefficient, generally first order approach is used. In other words, summation of the drag on individual components of the structure gives the total drag. Also, considerable sheltering and interaction between these components can change the drag which depend on many factors such as orientation and spacing of the components.

$$F = \frac{1}{2} C_d \rho A U^2 \qquad (2.1)$$

Wave forces on a stationary submerged object are drag and inertial forces. Also, these are expressed by Morison equation (Equation 2.2). In this equation, F_a denotes additional force required to accelerate the fluid around the object where V uttered displaced volume and C_m is the added mass coefficient.

$$F = F_d + F_a = \frac{1}{2}\, C_d \rho A u^2 + C_m \rho V \frac{\partial u}{\partial t} \qquad (2.2)$$

Morison equation is used for farm motion modelling. It also represents the structure with a series of components and forces them with parameterized loads based on the local hydrodynamics. Stresses and motions of shellfish farm components have been computed with the model. Figure 2.7 is given as an example for the model.

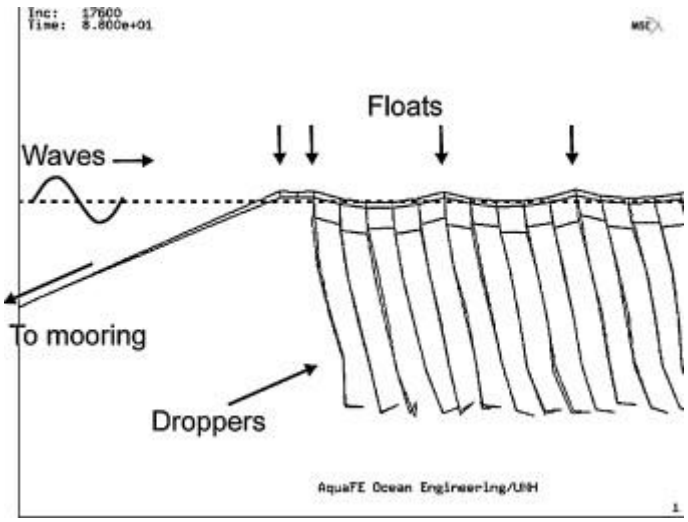

Figure 2.7. Model of a longline being forced by surface waves (Stevens et al., 2008).

Falnes (2002) (as cited in Stevens et al., 2008) expressed that the combination of wave forces acting on the submerged crop, buoyancy and moorings gives total force on the structure. The crop forms biggest part of the structure so it is subjected to most of the loadings. On the other hand, forces acting on mooring lines depend on the configuration of the structure. Also, forces can be estimated with appropriate coefficients C_d and C_m. Drag coefficients for steady flow are not proper because they are calculated by means of maximum horizontal water particle velocity. In addition, for heavily roughened piles in the absence of a current Wolfram and Naghipour (1999) (as cited in Stevens et al., 2008) suggested that to use $C_d = 1.7$ and $C_m = 2.0$.

Actual force on shellfish culture structures is determined by the relative velocity between structure and fluid. Besides, there are additional inertial forces related to the acceleration of the moving structure. However, motion of the structure is small with respect to wave orbital motion. Ocean wave conditions rarely composed of a single wave component. Waves are generally found in groups therefore there are periods of intense wave activity and this increases periods of wave breaking. This is probably to influence forcing of the longline.

Shellfish structures are only confined by their weight and drag and successfully being connected to the structure near the surface with a freely rotating pin. According to the case studies, due to the significant amount of rise and fall of the tide, there are mooring tension can be observed in inshore

location. If there is oscillating wave forces, summation of individual drag forces which also suggests a total tide-induced load increase. On the other hand, experimental studies offer that there may be existing vertical motion and vertical components of this force balance need to be considered.

Fredriksson et al. (2004) have studied on specification of four-cage mooring system geometry, subsurface flotation and pretension requirements by using analytical techniques. With standard analytical approach hydrostatic and geometric structure of the submerged grid mooring is estimated. Also, tension loads in the anchor legs and the desired geometry of the system can be calculated. To relatively easy diver serviceability, pre-tensioned subsurface grid at depth of 15 m is necessary for the four-grid mooring structure. For instance, due to average depth of water is 52 m, the grid plane is nearly 37 m off the bottom which is expressed as d_v. Besides, anchor legs are made of both rope (l_r) and chain (l_c); then they are not identical. Subsequently, for four side anchor legs, 27.4 m of chain and 78 m of rope are used. Anchor leg length to depth ratio is 2.9 for four side anchor legs while for eight corner legs it is 3.1. The horizontal component of anchor legs (d_H) is decided as 107 and 96 m, by assuming that the grid lines are 65 m. In addition, sketch of the anchor leg definition is given in Figure 2.8. By using these values, the static pre-tension and the geometry of submerged grid mooring can be computed.

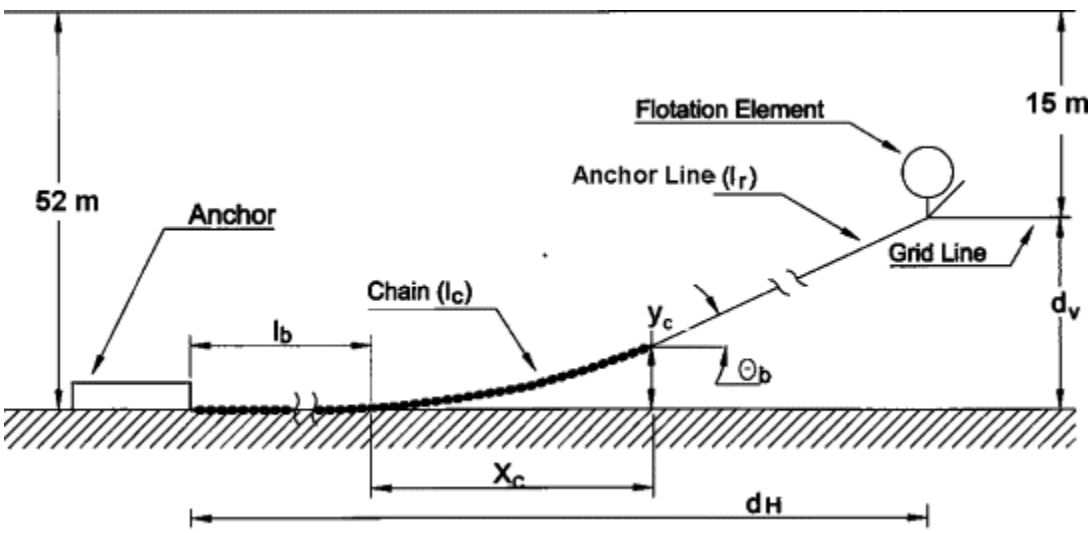

Figure 2.8. Definition sketch of anchor leg (Fredriksson et al., 2004).

To analyse the mooring, numerical model is used which is based on finite element analysis approach. Generally, wave and current loadings on truss, buoy and net elements drive the system dynamics. In this model, hydrodynamic forces on structural elements are calculated with modification of Morison equation which includes the relative motion between the structural element and the surrounding fluid. Haritos and He (1992) (as cited in Fredriksson et al., 2004) expressed this fluid force by using Equation 2.3.

$$\boldsymbol{f} = C_1\boldsymbol{V}_{Rn} + C_2\boldsymbol{V}_{Rt} + C_3\tilde{\mathrm{V}}_n + C_4\tilde{\mathrm{V}}_{Rn} \qquad (2.3)$$

In the above equation $V_{Rn}$and V_{Rt} are the normal and tangential components of the fluid velocity relative to the structural element. Normal component of total fluid acceleration is expressed as $\tilde{\mathrm{V}}_n$ and normal component of this is showed as $\tilde{\mathrm{V}}_{Rn}$. Bold letters mean vectors. Coefficients are calculated from $C_1 = 1/2\rho_w D C_n V_{Rn}$, $C_2 = C_t$, $C_3 = \rho_w A$ and $C_4 = \rho_w A C_a$, where D and A diameter and cross sectional area in deformed structure, ρ_w is the density of water, C_n and C_t are the normal and tangential drag coefficients. Also, $C_n$and $C_a$are dimensionless; however C_t has

viscosity dimension. Choo and Casarella (1971) (as cited in D.W. Fredriksson et al., 2004) expressed drag coefficients by Equation 2.4 and 2.5 as a function of Reynolds Number ($Re_n = \frac{\rho_w D V_{Rn}}{\mu,s}$ =-0.077215665+ ln (8/Re_n) and μ is the water viscosity).

$$C_n = \begin{cases} \frac{8\pi}{Re_n s}(1 - 0.87s^{-2}) & (0 < Re_n \leq 1), \\ 1.45 + 8.55Re_n^{-0.90} & (1 < Re_n \leq 30), \\ 1.1 + 4Re_n^{-0.50} & (30 < Re_n \leq 10^5) \end{cases} \tag{2.4}$$

and,

$$C_t = \pi\mu(0.55Re_n^{\frac{1}{2}} + 0.084Re_n^{2/3}) \tag{2.5}$$

Consequently, the consistent net element constructed considering the hydrodynamic forces acting on any section of netting and calculated with above equations for four-cage mooring system.

Fredriksson et al. (2008) investigated potential design procedures for closed containment aquaculture systems. In this study, for computation of fluid dynamics flow analysis is made. Due to wave currents fluid drag is considered and represented as;

$$F_{Drag} = \frac{1}{2}\rho A C_d V^2 \tag{2.6}$$

where mass density of water represented with ρ , area is showed as A, current velocity is represented as V and the drag coefficient denoted as C_d. Besides, by modeling the interaction between the fluid and the structure computational fluid dynamics (CFD) can be employed to determine drag coefficients. In this study, writers used ANSYS Fluent^{TM} which is based on Reynolds-averaged Navier Stokes approach.

Closed containment fish farm built in the CDF program, computational domain includes 44 units. As shown in Figure 2.9, the control volume discretized through an unstructured tetrahedral mesh and boundary surfaces defined by triangular elements. Mesh size on the containment surface is 1 m while mesh size of outer boundaries of the control volume is 20 m. In this modelling assumed that containment units and sea-floor are modelled as no-slip walls and walls of the free surface and side boundaries are with zero shear stress. Figure 2.9 reveals the three dimensional nature of the model. Besides, the nominal water depth is 20 m and the sea-bed is smooth and impermeable. Also deployment configuration includes walkways, mooring lines, waste containment piping and other topside structures. These components do not significantly affect the flow. Accordingly, they are not modelled.

A steady and uniform current is observed in the lengthwise direction. Then, simulations are performed by assuming the flow is from left to the right because drag coefficient is obtained based on the projected area of four containment units and drag coefficient values related with velocity. Besides, CDF approach is used to determine the flow characteristics through and around the farm. According to the experimental results, increase in velocity influence scouring effects on the bottom.

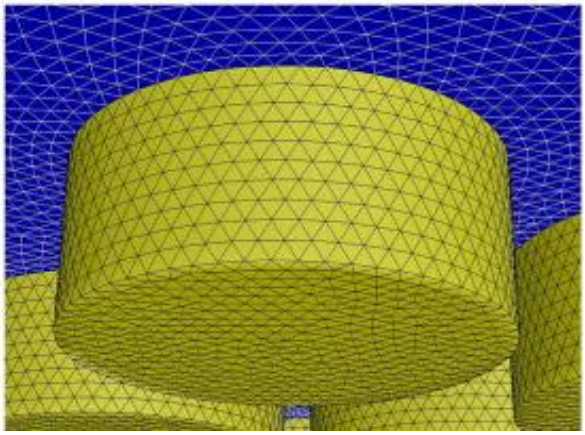

Figure 2.9. Three dimensional nature of the mesh (Fredriksson et al., 2008).

Modelling of tsunami damages to aquaculture facilities, e.g. marine vessels, is an important area for research and can help more accurate prediction of tsunami hazard and loss. The types of tsunami damage to marine vessels are: (i) grounding, (ii) stranding, (iii) failure of the mooring rope, (iv) loss of stability (Suppasri et al., 2013). In their study Suppasri et al. (2013) develops loss functions for tsunami damage to small marine vessels using the data for approximately 20,000 small marine vessels damaged by the 2011 Great East Japan tsunami. The loss functions consider the vessel type, tonnage, and distance from the tsunami source. It was found tsunami height greater than 2 m or flow velocity exceeding 1 m/s result in significantly higher damage probabilities. The results of the study also indicate that marine vessels located at further distances to the tsunami source experiences less damage mainly due to the reduced wave heights and flow velocities (i.e. smaller tsunamis with slower arrival times) at these locations, giving more time for evacuation, hence increasing their chance of survival with less damage.

In conclusion, elevation of water level, speed and acceleration of current are main design parameters of stability and safety of aquaculture plants. Increasing water elevation causes uplift motion of plant and exerts uplift force as tension on connecting chains to anchorage. The current causes drag, and acceleration causes inertia force on the supporting elements to anchorages of offshore aquaculture plants. During a tsunami, increasing water elevation, current speed and acceleration are observed. Therefore these parameters under tsunami motion are important for aquaculture plants. However since tsunami is a long wave the acceleration is less critical comparing to current speed and water elevation.

2.6 References

Choo, Y.I., and Casarella, M.J. (1971) “Hydrodynamic resistance of towed cables”. J. Hydronautics. 126–131.

Columbia Encyclopedia Definition of Aquaculture – Retrieved on 20 November 2014 from http://www.answers.com/topic/aquaculture

Falnes, J. (2002). “Ocean Waves and Oscillating Systems”. Cambridge University Press, UK, 275, pp. 5.

FAO Fisheries and Aquaculture Department: Global Aquaculture Production, Fishery Statistical Collections – Retrieved on 20 November 2014 from http://www.fao.org/fishery/statistics/global-aquaculture-production/en

FAO (2005) [RAP Publication 2005/09] Consortium to Restore Shattered Livelihoods in Tsunami-Devastated Nations (CONSRN), "Regional strategic framework for rehabilitation of fisheries and aquaculture in tsunami affected countries in Asia". 22 pp. Available at: http://www.fao.org/3/a-ae548e.pdf

FAO (2006) [RAP Publication 2006/08] Regional workshop, "One year later – The rehabilitation of fisheries and aquaculture in coastal communities of tsunami affected countries in Asia". 33 pp. Available at: http://www.fao.org/3/a-ag091e.pdf

FAO (2007) [RAP Publication 2007/19] "An overview of the impact of the tsunami on selected coastal fisheries resources in Sri Lanka and Indonesia". 44 pp. Available at: http://www.fao.org/3/a-ai000e.pdf

FAO (2014a) 2012 Yearbook on Fishery and Aquaculture Statistics. Prepared by the Statistics and Information Branch, Fisheries and Aquaculture Department, FAO, on the basis of information available as of 31 December 2013. Rome. 105 pp. Available at: http://www.fao.org/3/478cfa2b-90f0-4902-a836-94a5dddd6730/i3740t.pdf

FAO (2014b) The State of World Fisheries and Aquaculture: Opportunities and challenges. Rome. 223 pp. Available at: http://www.fao.org/3/contents/d1eaa9a1-5a71-4e42-86c0-f2111f07de16/i3720e.pdf

FAO (2014c) Fisheries and aquaculture emergency response guidance. (Edited by Cattermoul, B.; Brown, D. & Poulain, F.) Rome. 167 pp. Available at: http://www.fao.org/3/a-i3432e.pdf

Fredriksson, D. W., DeCew, J., Swift, M. R., Tsukrov, I., Chambers, M. D., and Celikkol, B. (2004). "The design and analysis of a four-cage grid mooring for open ocean aquaculture". Aquacultural Engineering, 32(1), 77-94.

Fredriksson, D. W., Tsukrov, I., and Hudson, P. (2008) "Engineering investigation of design procedures for closed containment marine aquaculture systems". Aquacultural Engineering, 39(2), 91-102.

Fullerton, B., Swift, M. R., Boduch, S., Eroshkin, O., and Rice, G. (2004) "Design and analysis of an automated feed-buoy for submerged cages". Aquacultural Engineering, 32(1), 95-111.

Haritos, N., and He, D.T. (1992) "Modelling the response of cable elements in an ocean environment". Finite Elements Anal. Design, 19, 19–32. 4.

NOAA Aquaculture Office: What is Aquaculture? – Retrieved on 20 November 2014 from http://www.nmfs.noaa.gov/aquaculture/what_is_aquaculture.html

Otsuka, K., Katoh, H., Satoh, K., and Fujima, K. (2009) The behavior of Tsunami-induced driftage and it's problem in the fishing areas. Research Rep. Japanese Institute of Fisheries Infrastructure and Communities, The Japanese Institute of Fisheries Infrastructure and Communities, Tokyo, Vol. 21, 127-130 (in English). Available at: http://www.jific.or.jp/dispatch/ronbun/pdf_h21/2120.pdf

Stevens, C., Plew, D., Hartstein, N., and Fredriksson, D. (2008) "The physics of open-water shellfish aquaculture". Aquacultural Engineering, 38(3), 145-160.

Suhey, J. D., Kim, N. H., and Niezrecki, C. (2005) "Numerical modeling and design of inflatable structures—application to open-ocean-aquaculture cages". Aquacultural Engineering, 33(4), 285-303.

Suppasri, A., Muhari, A., Futami, T., Imamura, F., and Shuto, N. (2013) "Loss Functions for Small Marine Vessels Based on Survey Data and Numerical Simulation of the 2011 Great East Japan Tsunami". Journal of Waterway, Port, Coastal, and Ocean Engineering, 140(5).

Wikipedia: Aquaculture – Retrieved on 20 November 2014 from http://en.wikipedia.org/wiki/Aquaculture

Walsh, M. L. and Hanafusa, K. (2013) "Two Years After: Post-Tsunami Recovery of Fisheries and Aquaculture in Northeastern Japan". World Aquaculture Magazine, June 2013, pp. 20-24. Available at: http://beta.was.org/Magazine/2013/02/files/assets/basic-html/page22.html

Wolfram, J., and Naghipour, M. (1999) "On the estimation of Morison force coefficients and their predictive accuracy for very rough circular cylinders". Appl. Ocean Res. 21, 311–328.

World Bank (2012) Learning from megadisasters: knowledge notes, Knowledge Note 6-3: Economic Impacts, in Cluster 6: The economics of disaster risk, risk management, and risk financing. Available at: https://wbi.worldbank.org/wbi/Data/wbi/wbicms/files/drupal-acquia/wbi/drm_kn6-3.pdf

World Fishing and Aquaculture (April 2010) – Retrieved on 25 November 2014 from http://www.worldfishing.net/news101/regional-focus/tsunami-destroys-chiles-fishing-industry

Yalciner, A. C., Suppasri, A., Mas, E., Kalligeris, N., Necmioglu, O., Imamura, F., Ozer, C., Zaytsev, A., Synolakis, C., Takahashi, S., Tomita, T., and Yon, G. (2011) "Field Survey on The Coastal Impacts of March 11, 2011 Great East Japan Tsunami", Abstract NH11A-1360 presented at 2011 Fall Meeting, AGU, San Francisco, Calif., 5-9 Dec.

CHAPTER 3. TSUNAMI-IMPACT ON COASTAL ECOSYSTEMS AND MARINE PROTECTED AREAS

3.1 Introduction

Large tsunamis are major geomorphic crises, since they imply extensive erosion, sediment transport and deposition in a few minutes and over hundreds of kilometres of coast (Paris et al., 2009). Such events have the potential to transform considerably the morphology, the sedimentary dynamics and consequently impact the coastal and near shore environments, its natural habitats and the biodiversity present therein. The main factors of perturbation for the marine ecosystems result from high wave energy and associated run-up, but more intensively by backwash processes, such as the large scale introduction of sediments from silts to pebbles, high levels of organic matter, human and natural debris, contaminants of different sorts (contained hazardous chemicals, oils, paints, freons, cleansers) which can then enter the trophic chains. These stressing factors do not have the same impact on the nearshore and coastal ecosystems as their resilience and recovery rate is a function of its intrinsic nature. The recovery of these ecosystems after a catastrophic tsunami event is fundamental for the future of marine resources and consequently to mitigate the socio-economic impacts on the affected regions, specially industries such as turism and coastal fishing.

The existing literature focuses more on the services provided by coastal ecosystems in the hazard mitigation and risk management (Cochran et al., 2007) than on the direct and indirect impacts that tsunamis have on those ecosystems. Numerous scientific studies illustrate that coastal ecosystems are important in protecting the coast against normal and extreme wind-driven waves, including cyclonic storm surges, less is known few studies have taken account of the high variability in the energy and speed of tsunami waves along different coastline stretches, making it difficult to compare the role of ecosystems in different regions. Despite these limitations those authors examine the influence of coastal vegetation in severely affected parts of Aceh and Southern Thailand during the 2004 tsunami. Their main conclusions point for a complex influence of coral reefs on tsunami waves, where lateral continuity is a critical factor. While some protection can be given by continuous lines of coral reefs, fragmented barriers may provide channeled waterways causing acceleration causing even greater destruction on land. Seagrass belts In contrast, according to the same study seems to provide more protection against tsunamis. Mangroves and other vegetation probably provided some protection against the 2004 tsunami; in numerous other locations, however, vegetation provided no protection or may in some cases even have increased the hazard (e.g. by contributing to flow debris, or by channelling water flows).

The impact of tsunami on reefs, seagrasses and mangroves, varies significantly and is also a function of the wave energy these ecosystems are normally exposed to. Areas impacted by strong storm surges, and big swells are likely more resilient to tsunamis than sheltered areas. Damage by wave energy is also species specific. Some species of coral, algae and other marine invertebrates are extremely delicate and cannot withstand turbulent high energy environments. As a result, these species would be particularly susceptible to the damaging wave energy generated by a tsunami.

Powerful tsunami can substantially alter some shallow water benthic habitats, reducing their effectiveness as nurseries and shelters for fish and benthic organisms. As a result, some near-shore fisheries can be impacted by very low recruitment success over the next few years. Unfortunately, such impacts could ripple through the entire food chain for decades, however, they will not likely cause lasting impacts.

Studying the impacts on the Acehenese reefs, following the Sumatra-Andanaman tsunami, Baird et al, (2005), verified that the damage to corals was generally confined with no significant change in

coral assemblages. Direct tsunami damage was dependent on habitat and restricted to corals growing in unconsolidated strata. They further verified that the reefs had little to no impact on damage on land, and that reef condition, prior and after tsunami impact, were more a function of initial vulnerabilities caused by fisheries that resulting from the tsunami itself. In these vulnerable areas, the authors report that corals were already reduced and substituted by high algal cover.

In this chapter we investigate the tsunami impact on ecosystems located along the coast of Portugal. We use tsunami numerical modelling together with the most credible earthquake scenarios in the southwest Iberia Margin region to estimate the tsunami impact on site-specific coastal ecosystems.

3.2 Estimating the tsunami impact on coastal ecosystems along the coast of Portugal-NE Atlantic region

a. Ecosystems along the coast of Portugal

Various types of coastal ecosystems exist along the coast of Portugal. Figure 3.1 depicts the distribution of the ecosystems in Portugal. The Portuguese National Network of Protected Areas distinguishes between two main coastal ecosystem zones: the marine especial protected zones (ZPEs), and the marine sites of communitarian importance (SIC).

Figure 3.1. Distribution of the ecosystems in Portugal.

The **ZPEs** include eight protected areas, among them:

- *Lagoa de Santo André* is a coastal lagoon located in the southwest coast of Portugal mainland and is separated from the sea by a narrow strip of dunes (Figure 3.2.a). This lagoon is one of the most important national wetlands for birds, where 106 species of waterfowl are surveyed.

- *Lagoa da Sancha* is a coastal lagoon located in the southwest coast of Portugal mainland, North of Sines (Figure 3.2.b). This lagoon stands out as an important place in the autumnal migration of trans-Saharan passerine, and is a reproduction ground for species that are threatened in much of respective European distribution area.

- *Berlengas* is a group of rocky islands, Berlengas, Farilhões and Forcadas, located off the Portuguese west coast, northwest of Cape Carvoeiro. It is an important site of seabirds' reproduction (Figure 3.2.c) that is regularly used by some characteristic species of the northeast Atlantic.

- *Costa Sudoeste* is a marine protected area of the southwest coast of Portugal. It is one of the most important areas for the conservation of birds as an important migratory corridor for soaring birds, shorebirds and passerines trans-Saharan migrants. The hosted diversity (about 230 species of regular attendance and about 40 irregular or adventitious presence, including dozens of migratory species passing), and characteristics of some groups of populations, give it an unmatched value in the context of conservation of birds at national and international level.

- *Ria Formosa*: this large lagoon system is the most important wetland area in south of the Portugal mainland, for its diversity and structural complexity and is protected to the south by a series of barrier islands, separated by mobile bar, some fixed artificially establishing communication between the lagoon and the ocean. The Ria is one of the most important areas of the country for migratory birds (Figure 3.2.d).

Figure 3.2. Coastal ecosystem zones in Portugal: the marine especial protected zones (ZPEs).

The **SICs** gather a set of protected coasts (see Figure 3.3) including:

- Litoral Norte : this zone covers the north coast of Portugal, where it can be found sandbank and reefs with a remarkable diversity of seaweed.

- Peniche/Santa Cruz: the North of Peniche covers Atlantic salty meadows, and it is one of two areas where occur this habitat in the biogeographic Mediterranean region, and also reefs that are present along the coast.

- Arquipélago da Berlenga : located northwest of the Cabo Carvoeiro it is composed by the Berlenga and Farilhões rocky islands and also the marine area around. This place possesses reefs as well submerged and semi-submerge sea caves with fauna and flora communities in a good state of conservation.

- Arrábida / Espichel: the Arrábida/Espichel coast is under the Mediterranean climate and a strong component of the Atlantic. In general, presents shallow water areas well limited by the scarp coast and also the Setúbal and Lisbon canyons. The south orientation of the coastal offers protection to the north wind and curling. This fact promoted the reproduction and development of an elevated number of marine species, most of them rare in Portugal.

- Costa Sudoeste: the Southwest coast presents a vast diversity of coastal habitats such as reefs and submerged and semi-submerge sea caves. One example of a special and symbolic occurrence of fauna is related to the ecologic adaptation of the only otter population that uses marine environments in Portugal.

Figure 3.3. Coastal ecosystem zones in Portugal: the marine sites of communitarian importance (SIC).

b. Tsunami impact on ecosystems along the coast of Portugal

We investigate the tsunami impact on the ecosystems located in the Algarve coastal region, south of Portugal. We focus on the Ria Formosa lagoon that is considered as the most important wetland area in south of the Portugal mainland. It presents a complex morphology and is protected by a series of barriers Islands (Figure 3.4).

Lagoon - Ria Formosa , South of Portugal

Figure 3.4. Ria Formosa ecosystem lagoon located in the coastal area of Algarve, South of Portugal.

Tsunami sources

As tsunami sources in this study, we consider the most credible earthquake sources located in the southwest Iberia margin (SWIM) region (Omira et al., 2009, Duarte et al., 2010 see Figure 3.5). These tsunamigenic sources represent the scenarios able to generate large tsunamis in the region (Omira el al., 2009) with a significant tsunami impact along the southern coast of Portugal, where the Ria Formosa lagoon is located. The tsunami scenarios are the Gorringe Bank fault (GBF), the Marques de Pombal Fault (MPF), the Horseshoe Fault (HSF), the Cadiz Wedge Fault (CWF) (see Figure 2.5). Due to the faults orientations (strike angles) and the bathymetry of the region that constrain the tsunami energy distribution, the MPF is the scenario that steers significant tsunami energy towards the southern coast of Portugal. Here we focus on the tsunami impact caused by the tsunamigenic MPF scenario along the Ria Formosa lagoon ecosystem.

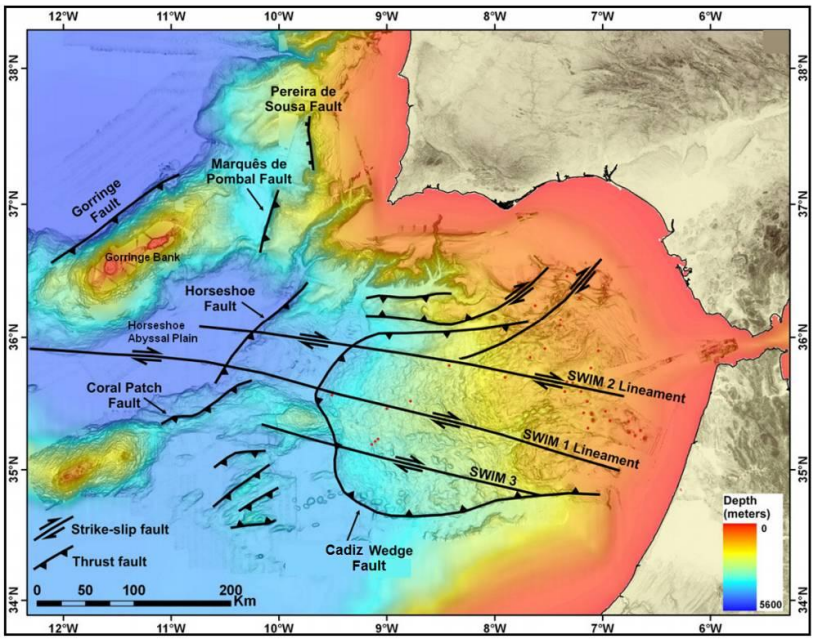

Figure 3.5. Map of active tectonic structures in the SWIM region (from Duarte et al., 2010)

Tsunami modeling

Tsunami impact on the ecosystems located along the southern coast of Portugal is investigated through numerical modeling. We perform numerical simulations of tsunami propagation and inundation using a validated numerical code (NSWING, Miranda et al., 2014) that solves the non-linear shallow water equations (Eq. 3.1 in Cartesian coordinates) using an explicit staggered leap-frog finite differences numerical scheme for linear terms and an upwind scheme for the non-linear terms. The code also employs a nested grid system, which allows a simultaneous calculation of tsunami propagation in open Ocean and inundation in targeted coastal zones. In the nested grid system, the inner (finer grid) region adopts a smaller grid size and time step and is nested inside an outer (larger grid) region. Here a system of three nested grids is used and the finer grid of 50 m resolution is considered to represent the Ria Formosa lagoon.

$$\frac{\partial \eta}{\partial t} + \frac{\partial P}{\partial x} + \frac{\partial Q}{\partial y} = -\frac{\partial h}{\partial t}$$

$$\frac{\partial P}{\partial t} + \frac{\partial}{\partial x}\left(\frac{P^2}{H}\right) + \frac{\partial}{\partial y}\left(\frac{PQ}{H}\right) + gH\frac{\partial \eta}{\partial x} + \tau_x H = 0 \qquad (3.1)$$

$$\frac{\partial Q}{\partial t} + \frac{\partial}{\partial x}\left(\frac{PQ}{H}\right) + \frac{\partial}{\partial y}\left(\frac{Q^2}{H}\right) + gH\frac{\partial \eta}{\partial y} + \tau_y H = 0$$

In the above equation set, η is the free surface elevation, h is the still water depth, H is the total water depth, P and Q are the volume fluxes in x and y directions respectively, τ_x and τ_y are the bottom frictional terms and g is gravity acceleration. The friction terms τ_x and τ_y are given in terms of the Manning's roughness coefficient n as (Eq. 3.2):

$$\tau_x = \frac{g\,n^2}{H^{\frac{7}{3}}} P \sqrt{P^2 + Q^2}\ ;\ \tau_x = \frac{g\,n^2}{H^{\frac{7}{3}}} Q \sqrt{P^2 + Q^2} \tag{3.2}$$

Impact on coastal ecosystem: Algarve-South of Portugal

The tsunami impact on the Ria Formosa lagoon is evaluated by deriving high-resolution tsunami inundation and current velocity along the coastal area of interest.

Figure 3.5 depicts the results of modeling tsunami impact on the Ria Formosa coastal ecosystem. This impact is assessed through wave heights and maximum flow depths distributions. Numerical modeling results clearly show the significant impact caused by the occurrence of a tsunami in the SWIM region on the costal ecosystems located along the southern coast of Portugal. Tsunami waveforms computed in some locations close the ecosystem barriers islands (Figure 3.6) indicate tsunami amplitudes up to 3m. Inundation map (Figure 3.6) shows that the incoming tsunami waves overtopped the sandy protection barriers and flood the entire lagoon of Ria Formosa with flow depths ranging from 1 m up to 3 m. Waveforms in some points located inside the lagoon indicate tsunami amplitudes reaching 1m.

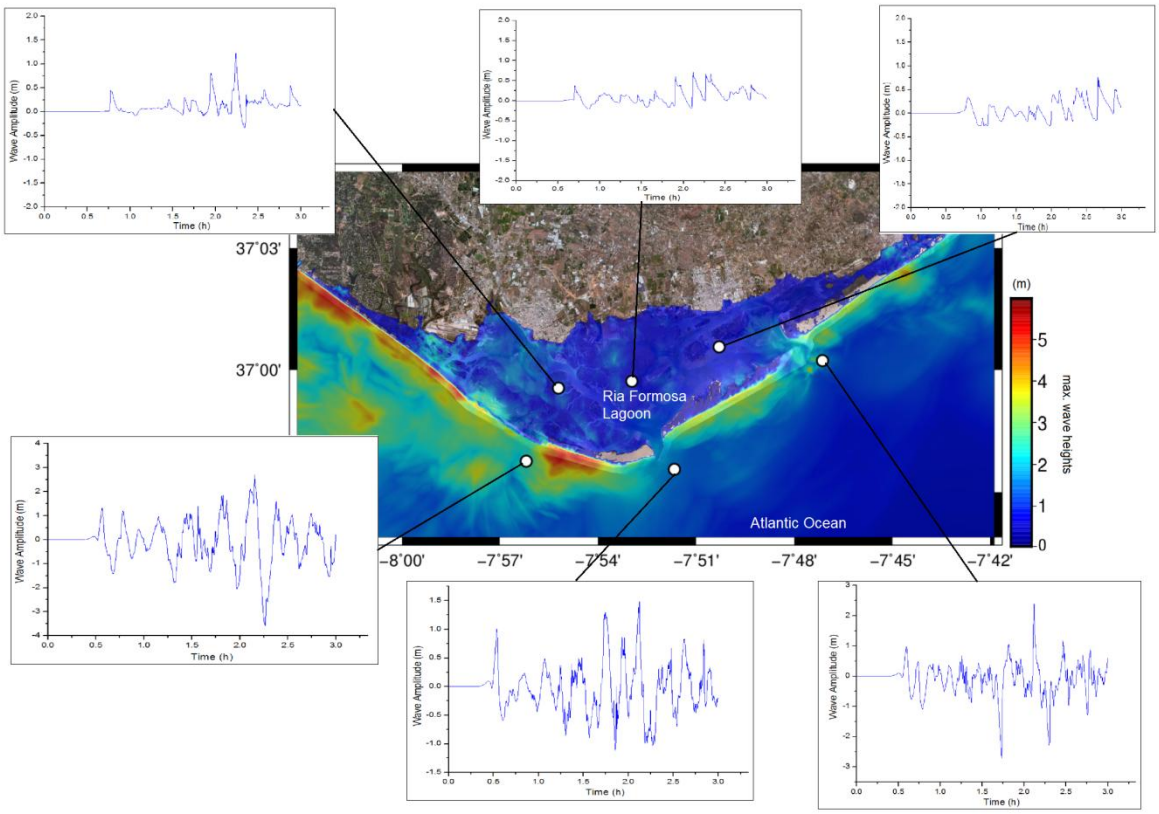

Figure 3.6. Impact of tsunami in the Ria Formosa lagoon caused by the MPF tsunamigenic scenario.

The tsunami flow velocity is recognized as an important hazard factor controlling the impact on marine ecosystems. Here, we simulate the tsunami flow velocity at the Ria Formosa lagoon considering the MPF scenario. The figure 3.7 depicts the computed maximum current speed (in m/s) at the Ria Formosa lagoon. The results show velocities ranging from 2 m/s up to 10 m/s. Such a

powerful tsunami can substantially alter the morphology of the Ria Formosa lagoon and reduce its effectiveness as shelter for migratory birds.

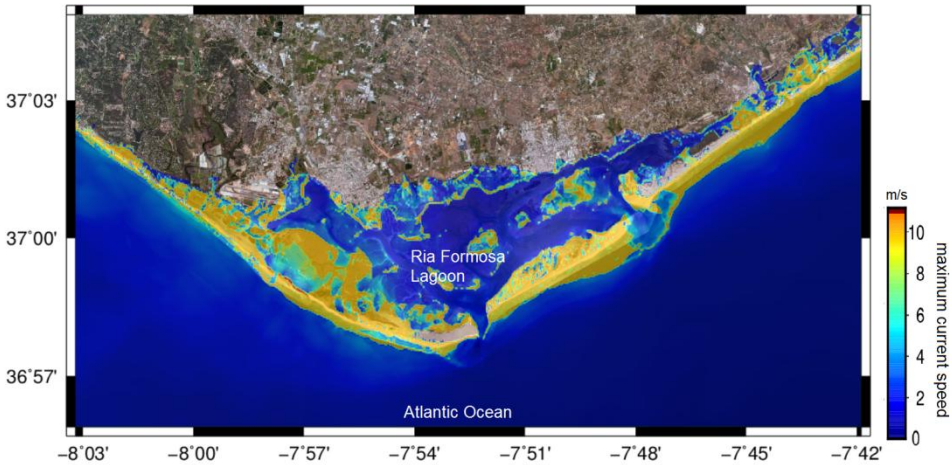

Figure 3.7. Maximum tsunami current velocities computed at the Ria Formosa lagoon considering the MPF tsunamigenic scenario.

3.3 Conclusions

In this chapter the tsunami impact on coastal ecosystems is carried using numerical modeling. The Ria Formosa lagoon, one of the most important costal ecosystems of Portugal, is taken as case study to perform high resolution tsunami impact. Active earthquake faults located in the southwest Iberia Margin are considered as the main tsunamigenic sources able to cause significant tsunami impact along the coast of interest.

Simulation results show that the Ria Formosa lagoon can suffer dramatic tsunami impact due to the occurrence of a tsunami event in the SWIM region. The high values of computed wave amplitudes, tsunami current velocities, and inundation extent clearly highlight the possibility of substantial alteration in the morphology of the Ria Formosa lagoon. Therefore, such a powerful impact will reduce the effectiveness of the lagoon as a shelter. To mitigate such a significant tsunami impact on ecosystems along the coast of Portugal, tsunami-protective measures must be initiated in the areas highly vulnerable to tsunami threat.

3.4 References

Baird, A. H., Campbell, S.J., Anggoro, A.W., Ardiwijaya, R. L., Fadli, N., Herdiana, Y., Kartawijaya, T., Mahyiddin, D., Mukminin,A.,Pardede, S.,T., Pratchett,M.S., Rudi, E. And Siregar, A. M. (2005). Current Biology, vol15, 1926-1930.

Cochard, R., Ranamukhaarachchi, S.L., Shivakoti, G.P., Shipin, O.V., Edwards, P.J., Seeland, K.T. (2007). The 2004 tsunami in Aceh and Southern Thailand: a review on coastal ecosystems, wave hazards and vulnerability. Perspectives in Plant Ecology, Evolution and Systematics. Volume 10, Issue 1, Pages 3‑40doi:10.1016/j.ppees.2007.11.001.

Duarte, J., Terrinha, P., Rosas, F., Valadares, V., Pinheiro, L. M., Matias, L., Magalhães, V., Roque, C. (2010) Crescent-shaped morphotectonic features in the Gulf of Cadiz (offshore SW Iberia). Marine Geology, 271, 236- 249.

Miranda J.M., Luis J., Reis C., Omira R., Baptista M.A : Validation of NSWING, a multi-core finite difference code for tsunami propagation and run-up. American Geophysical Union (AGU) Fall Meeting, San Francisco. Paper Number : S21A-4390. Session Number and Title: S21A, Natural Hazards, 2014.

Paris, R., Wassmer, P., Sartohadi, J., Lavigne, F., Barthomeuf, B., Desgages, E., Grancher, D., Baumert, P., Vautier, F., Brunstein, D., Gomez, C., (2009). Tsunamis as geomorphic crises: Lessons from the December 26, 2004 tsunami in Lhok Nga, West Banda Aceh (Sumatra, Indonesia), Geomorphology, Volume 104, Issues 1–2, Pages 59-72, ISSN 0169-555X, http://dx.doi.org/10.1016/j.geomorph.2008.05.040.

Omira R, Baptista M A, Matias L, Miranda J M, Catita C, Carrilho F, Toto E (2009) Design of a Sea-level Tsunami Detection Network for the Gulf of Cadiz. Nat. Hazards Earth Syst. Sci. 9: 1327-1338. http://www.nat-hazards-earth-syst-sci.net/9/1327/2009/nhess-9-1327-2009.html.